Available online at www.keaipublishing.com/en/journals/journal-of-magnesium-and-alloys/

ScienceDirect

Journal of Magnesium and Alloys 13 (2025) 3564–3595

www.elsevier.com/locate/jma

Review

Current status and perspectives on design, fabrication, surface modification, and clinical applications of biodegradable magnesium alloys ☆

Jianzeng Ren [a,b,1], Zhou Jiang [a,b,1], Jianbing He [a,b], Xiaoying Wang [a,b], Weihong Jin [a,b,c,*], Zhentao Yu [a,b,*]

[a] *Institute of Advanced Wear & Corrosion Resistant and Functional Materials, Jinan University, Guangzhou 510632, China*
[b] *College of Chemistry and Materials Science, Jinan University, Guangzhou 511436, China*
[c] *Shaoguan Research Institute of Jinan University, Shaoguan 512029, China*

Received 22 April 2025; received in revised form 5 July 2025; accepted 16 July 2025
Available online 19 August 2025

Abstract

Biodegradable metals have garnered considerable interest owing to their capacity for self-degradation following the repair of damaged tissues. This review commences with their historical development and clarifies the essential prerequisites for their successful clinical translation. Subsequently, a detailed review of magnesium-based materials is presented from five critical areas of alloying, fabrication techniques, purification, surface modification, and structural design, systematically addressing their progress in biodegradation rate retardation, mechanical reinforcement, and biocompatibility enhancement. Furthermore, recent breakthroughs *in vivo* animal experiments and clinical translation of magnesium alloys are summarized. Finally, this review concludes with a critical assessment of the achievements and challenges encountered in the clinical application of these materials, and proposes practical strategies to address current limitations and guide future research perspectives.

Keywords: Magnesium-based biodegradable metals; Alloying; Fabrication techniques; Purification; Surface modification; Structural design.

1. Introduction

With increasing lifespan and accelerating population aging, age-related skeletal and cardiovascular diseases have risen [1]. Implantable devices have emerged as a foundation of surgical strategies to address these conditions, enabling partial or complete substitution of impaired tissues and organs to achieve clinical benefits. Consequently, the clinical demand for various implants continues to increase. Ideal implant materials are characterized by a suite of critical properties including superior biocompatibility, adequate mechanical robustness, sustained stability, and tailored functionality [2]. Among these, biocompatibility, regarded as the capacity of a material to execute its intended function within a specific application while eliciting an appropriate host response [3], stands as the primary standard. Accordingly, the chemical composition of implants must exhibit non-toxicity and prevent adverse cellular or tissue reactions. Furthermore, mechanical strength must be sufficient to withstand the dynamic stresses and strains exerted by routine physiological activities, particularly when considering the effects of movement. Stability necessitates secure anchorage within surrounding tissues to mitigate displacement under external forces, while functionality mandates that implants deliver biomechanical reinforcement to both defective sites and regenerating tissues [4].

Implant materials employed in clinical applications are broadly categorized into two types according to their

☆ Peer review under the responsibility of Chongqing University.

* Corresponding authors at: Institute of Advanced Wear & Corrosion Resistant and Functional Materials, Jinan University, Guangzhou 510632, China.
E-mail addresses: whjin2@jnu.edu.cn (W. Jin), ninyzt@163.com (Z. Yu).

[1] Both authors contributed equally to this work.

https://doi.org/10.1016/j.jma.2025.07.006

biodegradation behavior: non-biodegradable and biodegradable materials. Non-biodegradable implants, designed for permanent integration within the body as tissue substitutes, predominantly consist of titanium alloys, cobalt-chromium alloys, and stainless steel [5]. These materials are characterized by outstanding biocompatibility, superior wear resistance, and high corrosion resistance, ensuring long-term structural integrity *in vivo* [6]. Nevertheless, the concept of permanent tissue replacement does not address conditions where temporary assistance is sufficient until complete tissue regeneration is achieved. Such limitations lead to implant failures due to mechanical factors, including stress shielding, migration, and wear debris, and biological complications, such as foreign body responses and bacterial infection [7]. Currently, the dependence on secondary surgical procedures for implant retrieval remains widespread, highlighting the need for alternative strategies. To this end, the development of biodegradable implant materials has attracted increasing attention.

The underlying principle of biodegradable implants focuses on materials engineered to gradually degrade *in vivo*, with biodegradation byproducts promoting tissue regeneration while reducing immunogenic responses. Upon completing their function in supporting tissue repair, these implants fully dissolve, eliminating the need for explantation procedures [8]. Biodegradable implants include polymers, ceramics, and metals. Biodegradable polymers, such as chitosan, silk fibroin, and fibrinogen, have been thoroughly investigated for their significant biodegradability, bioactivity, and biocompatibility. However, there are also some challenges including high solubility, insufficient mechanical properties, and potential denaturation during processing [9–11]. Conversely, biodegradable ceramics such as tricalcium phosphate and dicalcium phosphate undergo progressive dissolution through solution-mediated and cell-driven mechanisms, eventually being replaced by newly formed lamellar bone tissue. While these ceramics demonstrate outstanding biocompatibility and mechanical compatibility, their application is limited by reduced fracture toughness, brittleness, and excessive rigidity [12]. Fortunately, biodegradable metals offer enhanced mechanical properties, providing reliable temporary support capable of enduring applied loads. Their regulated biodegradation in the physiological environment effectively eliminates the risks associated with prolonged retention of non-biodegradable implants [13]. Currently, magnesium (Mg), zinc (Zn), iron (Fe), and their alloys represent the most widely studied biodegradable metals. As essential elements critical to physiological balance, these metals have been confirmed through numerous studies to exhibit favorable biocompatibility with human cells and tissues [14–16].

1.1. Typical biodegradable metals

The characterization of biodegradable metals requires the assessment of candidate materials based on two principal criteria: biodegradability and biocompatibility [17]. Accordingly, the key components of biodegradable metals must consist of essential metallic elements that are metabolizable within the human physiological environment. Mg, Zn, and Fe stand out as prominent candidates for the development of biodegradable metal implants, owing to their status as essential nutrients integral to human physiology [18–20]. Mg acts as a cofactor for numerous enzymatic reactions and contributes to the stabilization of DNA and RNA structures, Zn is crucial in mediating biological functions especially its anti-inflammatory effects, and Fe enables oxygen transport and supports metabolic processes [21]. Presently, biodegradable metals are mainly categorized into three primary systems based on their metallic elements: Mg-based biodegradable metals (*e.g.*, Mg-Ca, Mg-Zn, and Mg-Sr alloys) [22–24], Zn-based biodegradable metals (*e.g.*, Zn-Mg, Zn-Ca, and Zn-Cu alloys) [25–27], and Fe-based biodegradable metals (*e.g.*, Fe-Mn, Fe-W, and Fe-C alloys) [28–30].

1.1.1. Mg-based biodegradable metals

Mg-based biodegradable metals have garnered significant attention as biodegradable implant materials due to their excellent biocompatibility and favorable mechanical properties (Fig. 1a). Previous studies have shown that Mg implants can promote osteogenesis, accelerate the repair of bone defects, and enhance angiogenesis, thus highlighting their potential for addressing complex cardiovascular pathologies [31].

The inaugural clinical application of Mg was reported in 1878, when Dr. Huse successfully employed Mg wires for hemostasis during surgery [32]. Subsequently, Heublein et al. [33] investigated the use of Mg-based alloys in cardiovascular stents in 1998, implanting them into the coronary arteries of a porcine model. Histological evaluation revealed no evidence of platelet aggregation or thrombus formation, confirming the suitability of Mg for cardiovascular stent applications. Furthermore, the mechanical properties of Mg, which closely resemble those of cortical bone, position it as an ideal material for fracture fixation [34]. In 2012, Kraus et al. [35] implanted Mg-based alloys into rat femurs, and micro-computed tomography (micro-CT) analysis at 24 weeks post-implantation revealed complete bone regeneration at the defect site. However, these implants exhibited immediate corrosion upon implantation, with surface pitting observed as early as the first week. This corrosion was characterized by progressive surface pitting and a volumetric reduction of approximately 1.2% per day, consistently accompanied by hydrogen gas release. The central challenge impeding the widespread application of Mg-based materials lies in their premature loss of mechanical integrity. While stable structural support is required throughout the entire 24–36 weeks bone regeneration process, most existing Mg-based alloys are completely resorbed before this endpoint, typically within 6–12 weeks. Consequently, they fail to provide the sustained support necessary for successful healing [36]. To improve clinical applicability, current research is focused on regulating the biodegradation rate to align with tissue regeneration timelines, minimizing hydrogen bubble formation and ensuring that ion release concentrations remain within physiologically tolerable limits.

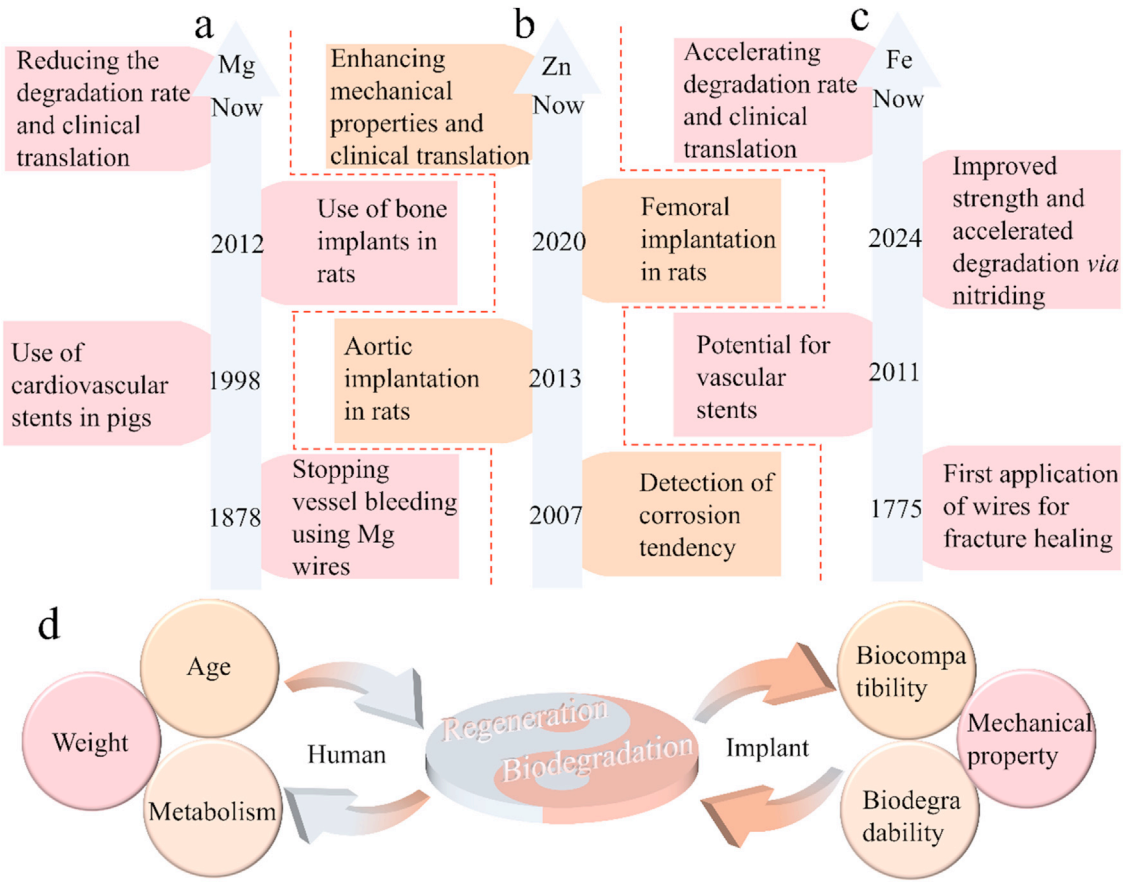

Fig. 1. Historical development of biodegradable metals: (a) Mg, (b) Zn, and (c) Fe; (d) key factors influencing the balance between tissue regeneration and implant biodegradation.

1.1.2. Zn-based biodegradable metals

In contrast to Mg-based biodegradable metals, Zn-based biodegradable metals have emerged as a relatively recent addition to the field (Fig. 1b). These materials are regarded as promising candidates for biodegradable implants owing to their outstanding biocompatibility, suitable biodegradation kinetics, and facile fabrication processes [37].

Initial investigations into Zn-based biodegradable metals began in 2007, with early electrochemical polarization studies demonstrating a distinct corrosion tendency compared to other inert biomedical alloys [38]. Subsequent research has revealed that Zn-based metals attenuate the progression of atherosclerosis by modulating endothelial cell apoptosis, thereby establishing them as viable materials for biodegradable cardiovascular stents [39]. In 2013, Bowen et al. [40] reported that, following four months of pure Zn implantation into the aorta of rats, approximately 70% of the cross-sectional area remained intact, after which the biodegradation rate significantly increased, meeting the corrosion requirements essential for cardiovascular stents.

In the field of orthopedics, Zn-based biodegradable metals have attracted considerable interest due to their capacity to enhance osteoblast differentiation, while inhibiting osteoclast differentiation [41]. Jia et al. [42] implanted Zn-based alloys into rat femurs in 2020, and both micro-CT and histological evaluations demonstrated robust osteogenic activity. Mechanical testing further indicated an elongation of 84% and a tensile strength exceeding 200 MPa. Despite these improvements compared to pure Zn, the mechanical properties of Zn-based biodegradable metals are still insufficient for some load-bearing skeletal applications [38]. Consequently, current research efforts are primarily focused on enhancing their mechanical performance to broaden their applicability in medical implant scenarios.

1.1.3. Fe-based biodegradable metals

Fe-based biodegradable metals have attracted significant attention as biodegradable implant materials owing to their exceptional mechanical properties and outstanding biocompatibility (Fig. 1c). Compared with other biodegradable metals, Fe-based alloys enable the fabrication of thinner clinical devices, such as cardiovascular stents, and precisely engineered porous scaffolds for bone regeneration.

The medical application of Fe dates back to its early use in wound closure and fracture stabilization [43]. In 1775, Icart et al. [44] pioneered the successful deployment of Fe wires to facilitate fracture healing in human subjects. Subsequently, Peuster et al. [45] implanted Fe stents into New Zealand white

rabbits, documenting low thrombogenicity, minimal inflammatory responses, and evidence of *in vivo* biodegradation. In 2011, Liu et al. [30] reported enhanced endothelial cell viability compared to smooth muscle cells when cultured on Fe-based biodegradable metals, underscoring their potential for vascular stent applications. In 2024, Zhang et al. [46] enhanced the mechanical robustness of Fe alloys by incorporating 0.05% nitrogen. This modification enabled a 76% reduction in Fe content for a given stent length, thereby shortening the stent's degradation period. Kraus et al. [47] implanted Fe-based alloys into rat femurs and, following a comprehensive 52-weeks evaluation, observed robust bone tissue regeneration accompanied by the formation of Fe oxide biodegradation products on the implant surface. Nevertheless, the biodegradation rate remains slow, primarily due to the impediment of oxygen transport caused by these corrosion products. Consequently, contemporary research efforts are focused on alloying strategies and surface modification techniques to mitigate the passivating effects of biodegradation byproducts, thereby accelerating biodegradation kinetics and enhancing the clinical viability and efficacy of Fe-based biodegradable metals.

1.2. Coupling of metal biodegradation and tissue regeneration rates

Biodegradability refers to the characteristic corrosion of biocompatible metals in the physiological environment. During this process, free ions are released from the metal substrate, diffusing into the surrounding bodily fluids, which consist of water, dissolved oxygen, proteins, and electrolyte ions such as chlorides and hydroxides [48]. Concurrently, the biodegradation byproducts in these fluids are expected to have beneficial effects on tissue regeneration. For example, Mg^{2+} has been shown to enhance osteoblast adhesion and proliferation. Ideally, under the influence of various factors, the biodegradation rate should be coordinated with the pace of tissue repair, while minimizing common adverse effects. Li et al. [49] have investigated the biodegradation behavior and osteogenic potential of Mg-2Zn-1Mn alloy in a rat femoral fracture model. Immersion assays reveal a consistent biodegradation profile for the alloy, while both *in vitro* and *in vivo* assessments confirm its outstanding tissue compatibility and significant ability to stimulate the differentiation of bone marrow mesenchymal stem cells (BMSCs) into preosteoblasts, thereby promoting bone formation and mineralization. Nevertheless, the biodegradation kinetics of materials in the physiological environment depend not only on their composition and microstructure but also on variables such as host-specific factors, intended application, and implantation site. This multifactorial dependency complicates the achievement of optimal alignment between the material's biodegradation rate and the dynamics of new tissue formation and substitution, representing the persistent challenge and critical barrier to the clinical translation of biodegradable metallic materials.

1.3. Mechanical dynamic regulation of metal biodegradation and tissue regeneration

Biodegradable metals are essential to provide continuous mechanical support throughout the tissue remodeling process, requiring their mechanical properties to evolve dynamically over the implantation duration. Ideally, these implants must maintain sufficient mechanical integrity until they are completely degraded and safely metabolized in the physiological environment. As tissue regeneration progresses, the implant gradually degrades, facilitating load transfer to the regenerating tissue and ensuring a seamless transition. For instance, Bowen et al. [50] have implanted pure Mg specimens into murine arteries. After 29 days post-implantation, the specimens remain visually intact and maintain good mechanical integrity. However, by day 32 post-implantation, the specimen fracture, likely due to the combined effects of uniform and localized corrosion and the typical stresses exerted by the arterial matrix. From a mechanical perspective, the specimens at 32 days are considered functionally degraded, with effective tensile strength and ductility reduced to zero. In the context of biodegradable bone implants, prolonged retention of mechanical integrity is crucial compared to bioresorbable stents, given that bone implants typically endure continuous loads and may encounter complex loading conditions. Wu et al. [51] have implanted Mg-based bone implants into the ulnae of New Zealand white rabbits, observing substantial callus formation surrounding the implants by 8 weeks, with most of the implant replaced by callus after implantation for 12 weeks. Newly formed bone bridges a 15 mm defect at 8 weeks and exhibits further maturation by 12 weeks, with three-point bending tests confirming adequate mechanical strength of the regenerated bone. Collectively, it is crucial to elucidate the dynamic biomechanical interplay between *in vivo* implant biodegradation and tissue regeneration and to leverage this understanding to guide the tuning of the material's initial microstructure and static mechanical properties.

1.4. Biocompatibility between metal biodegradation products and tissues

Biocompatibility is defined as the capacity of a material to integrate effectively with living tissues without triggering negative responses. For biodegradable metals, it is imperative that their biodegradation byproducts similarly prevent adverse host responses [52]. During biodegradation, the formation of solid metal salt precipitates, typically characterized by poor solubility in aqueous environments, poses challenges to their clearance from the body, potentially disrupting local homeostasis at the implantation site. For instance, compounds such as $MgCO_3$, $Mg_3(PO_4)_2$, $Zn(OH)_2$, $Zn_3(PO_4)_2$, and $Ca_3(PO_4)_2$, despite exhibiting low solubility in water, exhibit excellent biocompatibility in bone tissue. $MgCO_3$ is used as a component in bioglass, $Mg_3(PO_4)_2$ and $Ca_3(PO_4)_2$ are key ingredients in bone cements, and $Zn_3(PO_4)_2$ functions as a dietary supplement [53,54]. Furthermore, $Mg(OH)_2$, the predominant biodegradation byproduct of Mg-based biodegradable metals,

displays moderate solubility and can either gradually dissolve or react with Cl^- to yield soluble $MgCl_2$. In rabbit models, studies have confirmed that Mg^{2+} released from Mg-based implants are effectively assimilated *in vivo*. Additionally, an increase in the serum Ca^{2+} level has been noted, possibly due to localized Mg^{2+} accumulation promoting bone mineralization and thus stimulating osteogenesis while raising the systemic Ca^{2+} level [55]. Although recent research suggests that the biodegradation byproducts of biodegradable metals demonstrate excellent biocompatibility at the implantation site, further studies are needed to fully understand their impacts on tissues, cellular responses, and the broader physiological system. Achieving an optimal balance between tissue regeneration and biodegradation necessitates not only meticulous control over various material properties but also consideration of patient-specific factors, such as age, weight, and metabolic rate. This aspect is crucial in designing advanced biodegradable metal systems with excellent mechanical properties, biodegradability, and biocompatibility (Fig. 1d).

2. Current status of research and development of biomedical Mg-based biodegradation metals

2.1. Alloying

Alloying represents an effective strategy for enhancing the overall performance of a metal matrix through the incorporation of additional alloying elements. This approach improves the mechanical properties of the metal matrix by altering its microstructure. For instance, the dissolution of alloying elements in a single-phase microstructure results in solid solution strengthening, while the precipitation of a secondary phase induces precipitation hardening [56]. Moreover, alloying elements can influence the corrosion mechanisms, thereby altering the nature of the biodegradation byproducts of biodegradable metals. For example, the integration of alloying elements can promote the formation of a compact corrosion product layer on the surface of biodegradable metals, thereby inhibiting further corrosion progression [57]. Table 1 summarizes the research outcomes regarding the enhancement of mechanical properties and corrosion resistance in Mg-based biodegradable metals *via* alloying strategies.

Alloying substantially enhances both the mechanical properties and corrosion resistance of Mg-based biodegradable metals. However, in clinical settings, the concurrent dissolution of alloying elements with the metal matrix may induce harmful effects on the nervous system and osteoblast function. For instance, an excessive release of Al ions has been associated with the development of neurodegenerative disorders, such as dementia and Alzheimer's disease [58]. Meanwhile, excessive alloying elements may trigger galvanic corrosion between the Mg matrix and secondary phases, accelerating degradation of the matrix. Moreover, the cytotoxicity, resulting from alloying elements released during biodegradation, is closely related to the kinetics of the biodegradation process. Therefore, a comprehensive modulation of biodegradation dynamics must consider these diverse factors, and extensive, long-term *in vivo* studies may be necessary to fully assess the biosafety profile of alloyed biodegradable metals.

2.2. Fabrication techniques

In the field of materials science, a key tenet is the complex interplay between processing methodologies, microstructural evolution, and resulting material properties. Fig. 2 presents a comparative analysis of the microstructure, tensile fracture morphology, and biodegradation performance of WE43 alloys fabricated by traditional and advanced manufacturing processes [59,60]. Different fabrication techniques give rise to microstructures with unique attributes [57]. Employing distinct processing strategies to tailor/control material properties is a well-justified approach, which has been demonstrated and successfully implemented across a wide range of metallic systems.

2.2.1. Traditional manufacturing techniques

Amid ongoing advancements in materials processing, casting and powder metallurgy represent the most traditional techniques for the fabrication of Mg-based biodegradable metals. Casting involves introducing molten Mg-based alloys into molds, followed by cooling and solidification, making it highly suitable for large-scale production of standardized implants.

The incorporation of alloying elements such as Zn and Ca during casting can enhance both mechanical properties and biodegradation kinetics. However, this method is often hampered by the formation of porosity and inclusions, which compromise mechanical integrity and biodegradation uniformity, while providing limited control over alloy composition and microstructure.

Therefore, powder metallurgy has emerged as a favored approach due to its superior material utilization, precise control over performance, and fabrication versatility. These attributes are particularly beneficial for high-performance and patient-specific implants. This technique allows for precise control of composition and ensures microstructural homogeneity in Mg-based biodegradable medical implants, thereby producing outstanding mechanical properties and a tunable biodegradation rate that meets stringent biocompatibility criteria. Additionally, powder metallurgy enables the fabrication of intricate geometries such as screws and scaffolds, improving material efficiency and reducing production costs. The complete fabrication sequence typically includes powder atomization, mechanical alloying, isostatic pressing, sintering, and subsequent post-processing [83].

Despite the inherent advantages of powder metallurgy in optimizing efficiency and performance, the high reactivity of Mg predisposes it to oxidation, and the complexity of the process may impose practical limitations. Nevertheless, both casting and powder metallurgy have been instrumental in the development of Mg-based biodegradable metals, establishing a robust foundation for their use in medical implant applications. Table 2 summarizes the selected performance

Table 1
Mechanical properties, corrosion performance, and advantages of Mg-based biodegradable metals.

Materials	Ultimate tensile strength (MPa)	*In vitro* corrosion rate ($mm \cdot y^{-1}$)	Advantages	Ref.
Mg-1Zr	270	0.65	Zr-induced grain refinement improves corrosion resistance, preserves mechanical integrity, and enhances osteogenic activity by promoting cell proliferation while restricting osteoclast differentiation for modulated bone regeneration.	[61]
Mg-1Ca	239	N.A.	Mg-1Ca pins demonstrate gradual *in vivo* degradation and significant osteogenesis by the third month.	[62]
Mg-3Zn	225	2.3	Zn promotes osteogenic differentiation by upregulating key proteins related to osteogenesis.	[63]
Mg-5Ca	202.72	N.A.	Mg-5Ca demonstrates excellent yield strength and its extracts exhibit no cytotoxicity.	[64]
Mg-1Al-Cu	231	0.01	Cu doping enhances antibacterial properties.	[65]
Mg-2Zn-1Mn	243.5	0.36	Zn and Mn alloying promotes the formation of a denser corrosion product layer compared to pure Mg, thus enhancing barrier integrity.	[63]
Mg-0.45Zn-0.45Ca	N.A.	0.97	The alloy promotes bone healing and new bone formation in direct contact with corrosion products, while the alloy screw undergoes slow degradation and remains present after 24 weeks of implantation.	[66]
Mg-1Zn-0.6Sc	231	0.09	The addition of Sc induces grain refinement, which increases strength, and the formation of nano-scale ScZn phases with low electrochemical potential acts as micro-anodes, protecting the Mg matrix from corrosion.	[67]
Mg-1Ca-1Sr	230	N.A.	Incorporating Ca retards degradation by stabilizing the phase constitution and suppressing precipitation of the cathodic $Mg_{17}Sr_2$ phase, thereby mitigating micro-galvanic effects, and enhances BMSCs adhesion.	[68]
Mg-6Zn-0.5Zr	365	N.A.	The combination of fine, oriented recrystallized grains, a strong basal texture, and a high density of nano-scale precipitates imparts the alloy with an excellent strength-ductility balance.	[69]
Mg-1.8Zn-0.2Gd	272.2	0.12	Consisting of a single α-Mg phase, the alloy exhibits no internal micro-galvanic corrosion, which is comparable to high purity Mg, and demonstrates non-cytotoxicity to L929, MG63, and VSMC cells.	[70]
Mg-0.3Sr-0.5Y	111.53	0.82	The simultaneous solid solution of Y in both α-Mg and $Mg_{17}Sr_2$ phases reduces micro-galvanic corrosion.	[71]
Mg-0.5Zn-0.5Nd-6Sc	180	N.A.	The addition of Sc acts as a potent grain refiner to ensure appropriate mechanical properties in the cast alloy, while *in-situ* formed Sc_2O_3 provides a stable passivation layer on the Mg matrix.	[72]
Mg-1Zn-0.2Ca-4Ag	267	8.74	Ag addition strengthens the alloy by inducing the precipitation of the reinforcing $Ag_{17}Mg_{54}$ phase.	[73]
Mg-2.2Zn-3.7Ce-1.5Ca	192	6.9	Ca strengthens the Mg-2.2Zn-3.7Ce alloy by promoting precipitation of the $Ca_3Mg_xZn_{15-x}$ phase ($4.6 \leq x \leq 12$).	[74]
Mg-2Ca-0.5Mn-4Zn	189.2	N.A.	Zn addition induces precipitation of the $Ca_2Mg_6Zn_3$ phase at cathodic sites, enhancing mechanical strength but promoting localized galvanic corrosion. This detrimental effect is mitigated through formation of a protective Mg oxide surface layer.	[75]
Mg-4Zn-0.5Ca-0.16Mn	180	5.02	Dissolution of the eutectic $Ca_2Mg_6Zn_3$ phase enhances plasticity, while concurrent precipitation of strengthening Mg_4Zn_7 phases at Mn particle/matrix interfaces markedly increases yield strength.	[76]
Mg-Zn-RE-0.5Ca	N.A.	2.82	Addition 0.5 wt.% Ca reduces the corrosion rate, while increasing Ca content to 6 wt.% significantly elevates corrosion rate due to galvanic coupling effects.	[77]
Mg-1Zn-1Sn-0.2Sr	245	0.55	Doping with 0.2 wt.% Sr improves mechanical and corrosion performance through grain refinement and second-phase strengthening, while high hydrogen overpotential of Sn simultaneously suppresses hydrogen evolution reaction.	[78]
Mg-0.5La-0.3Ca-0.3Ge	N.A.	0.15	The significantly hindered degradation arises from a dense, protective GeO passivation layer.	[79]
Mg-3Sn-1Zn-0.5Mn	156	N.A.	Hot extrusion profoundly refines the grain structure, enhancing mechanical properties, corrosion resistance, and biocompatibility.	[80]
Mg-0.5Zn-0.35Zr-0.15Mn-1Sc-2Tb	172	N.A.	Sc and Tb solute additions refine grains while enhancing mechanical and corrosion performance. Subsequent degradation generates $Sc(OH)_3$ and $Tb(OH)_3$ byproducts that retard matrix degradation, while the released ions show no cytotoxicity.	[81]
Mg-6Zn-0.6Zr-0.4Ag-0.2Ca	389	N.A.	Severe plastic deformation *via* equal channel angular pressing refines grain size, imparting ultra-high strength. However, this process paradoxically induces embrittlement with low elongation while accelerating degradation.	[82]

N.A.: not available.

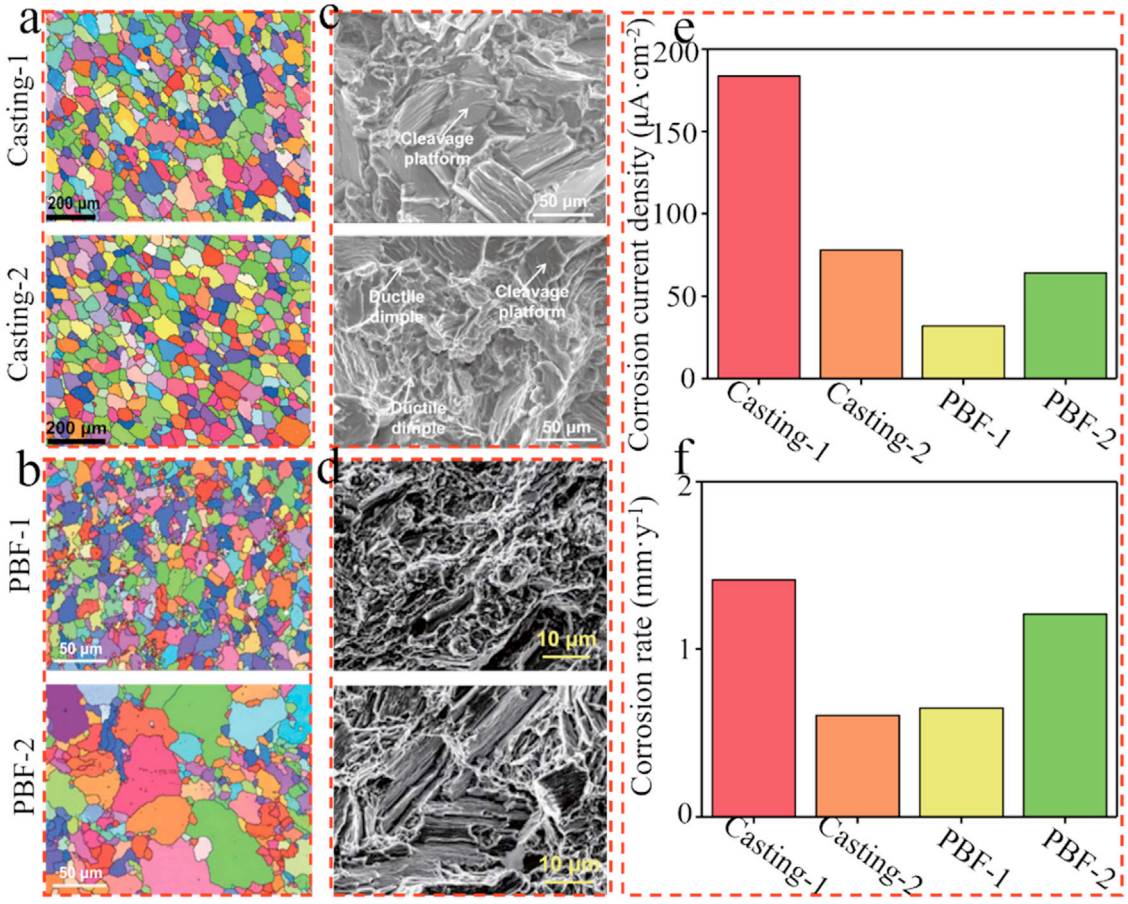

Fig. 2. Microstructure, tensile fracture surfaces, and corrosion behavior of WE43 alloy fabricated by casting and powder bed fusion (PBF) processes [59,60]: EBSD maps of (a) cast and (b) PBF-fabricated WE43 alloy; tensile fracture surfaces of (c) cast and (d) PBF-fabricated WE43 alloy; electrochemical corrosion results showing (e) corrosion current density and (f) corrosion rates for both cast and PBF-fabricated WE43 alloy. (Casting-1 and Casting-2 denote gravity cast and squeeze cast WE43 alloy, respectively; PBF-1 and PBF-2 refer to PBF-fabricated WE43 alloy processed under different parameters).

Table 2
Mechanical and biodegradation properties of Mg-based biodegradable metals prepared by casting and powder metallurgy.

Materials	Methods	Mechanical properties			Corrosion parameters			Ref.
		Yield tensile strength (MPa)	Tensile strength (MPa)	Elongation (%)	Corrosion potential (V)	Corrosion current density ($\mu A \cdot cm^{-2}$)	Corrosion rates ($mm \cdot y^{-1}$)	
Pure Mg	As-cast	N.A.	N.A.	N.A.	−1.78	14.60	0.33	[90]
Mg-1Si	As-cast	N.A.	N.A.	N.A.	−1.58	5.60	0.12	[90]
Mg-1Si-0.5Y	As-cast	N.A.	N.A.	N.A.	−1.64	3.24	0.07	[90]
Mg-2Si	As-cast	N.A.	N.A.	N.A.	−1.57	3.91	0.09	[90]
Mg-2Si-0.5Y	As-cast	N.A.	N.A.	N.A.	−1.53	4.98	0.11	[90]
Mg-2Ca	As-cast	N.A.	N.A.	N.A.	−1.64	10.54	N.A.	[91]
Mg-3Ca	As-cast	N.A.	N.A.	N.A.	−1.60	25.59	N.A.	[91]
Mg-1Ca	Powder metallurgy	147.78	217.28	14.36	−1.65	15.82	N.A.	[64]
Mg-5Ca	Powder metallurgy	183.32	202.72	9.03	−1.47	42.69	N.A.	[64]
Mg-10Ca	Powder metallurgy	119.63	200.25	7.74	−1.45	74.87	N.A.	[64]
Mg2Zn	Powder metallurgy	N.A.	150	7.2	−1.57	48	5.2	[92]
Mg2Zn-2Al_2O_3	Powder metallurgy	N.A.	160	9.8	−1.53	12	2.5	[92]
Mg2Zn-4Al_2O_3	Powder metallurgy	N.A.	170	8.5	−1.55	30	4.1	[92]
Mg2Zn-8Al_2O_3	Powder metallurgy	N.A.	191	4.4	−1.60	60	6.7	[92]

parameters of Mg-based biodegradable metals fabricated by casting and powder metallurgy.

2.2.2. Advanced manufacturing techniques

Additive manufacturing (AM) represents an advanced fabrication process for Mg-based biodegradable metals, offering precise control over microstructural characteristics. This capability enables grain refinement and optimization of phase composition, thereby enhancing both mechanical properties and corrosion resistance. Moreover, AM facilitates the integration of functional architectures such as internal channels and gradient materials into a single component, thereby promoting bone tissue regeneration and improving implant biocompatibility. Consequently, AM is widely recognized as a robust approach for fabricating metallic biomaterials. Common AM techniques include powder bed fusion (PBF) (Fig. 3a), binder jetting (BJ) (Fig. 3b), and directed energy deposition (DED) (Fig. 3c and d) [84].

PBF utilizes lasers or electron beams to selectively fuse metal powders layer by layer, thereby producing solid constructs [85]. The major approaches of PBF include selective laser melting (SLM), selective laser sintering (SLS), and electron beam melting (EBM). SLM is renowned for its high precision and energy efficiency. Li et al. [86] have reported that WE43 alloy scaffolds fabricated *via* SLM exhibit a refined grain structure and enhanced mechanical performance, with microstructural analysis revealing elongated grains at the top of the sample (denoted by dashed lines) (Fig. 3e) and transgranular crack propagation (Fig. 3f). Liu et al. [87] have achieved scaffolds with a relative density exceeding 99.5%, a compressive strength of 23 MPa, and a Young's modulus of 873 MPa through optimized energy input. Xie et al. [88] have demonstrated that SLM-processed Mg-Nd-Zn-Zr neither altered MC3T3-E1 cell morphology (Fig. 3g) nor inhibited cell viability (Fig. 3h). SLS partially melts powder particles, followed by re-solidification. Shuai et al. [89] have found that poly-L-lactic acid (PLLA)/Mg scaffolds produced via SLS exhibit a porous architecture with a Vickers hardness of 118.4 MPa. Li et al. [93] have observed that PLA/Mg scaffolds fabricated by SLS display a significantly increased biodegradation rate compared to pure PLA, with compressive strength reaching 5.6 MPa. EBM, performed under vacuum, reduces oxidation and compositional segregation. Zhang et al. [94] have demonstrated that the EBM-fabricated AZ31 alloy exhibit a refined grain structure, with yield strength and tensile strength increasing by 50% and 40%, respectively. Although EBM's energy efficiency and powder recyclability boost productivity, precise control of heat input is essential to prevent Mg evaporation.

BJ employs liquid binder deposition to bond powder particles. Cho et al. [95] have developed a full liquid-phase sintering process for WE43 alloy, yielding specimens with a porosity of 2.5% and notably enhanced corrosion resistance. Kuah et al. [96] have observed that the sintering temperature in BJ affects the porosity and corrosion rate, with higher temperatures reducing porosity yet increasing element evaporation.

DED utilizes focused thermal energy to deposit material layer by layer, proving effective for fabricating heterogeneous structures [97]. Wire arc additive manufacturing (WAAM), a prominent DED technique, deposits Mg alloys via laser or arc methods. Li et al. [98] have reported significant grain refinement in the WAAM-fabricated AZ31 alloy. Yang et al. [99] have demonstrated that AZ31 blocks produced by WAAM exhibit superior mechanical properties compared to cast equivalents. Guo et al. [100] have found that the WAAM-processed AZ80M alloy displays mechanical properties comparable to extruded materials, substantially outperforming cast counterparts. DED systems, characterized by operational simplicity, can be integrated with complementary manufacturing techniques, thereby broadening their applicability in Mg-based biodegradable metal applications.

2.3. Purification

During casting processes, Mg inevitably absorbs excessive gaseous and metallic impurities. Common metallic impurities in Mg alloys include Fe, Ni, and Cu. When the concentrations of these elements exceed their tolerance thresholds typically 35–50 ppm for Fe, 20–50 ppm for Ni, and 100–300 ppm for Cu (wt.%) [101], they significantly accelerate Mg corrosion. Metal purification involves removing detrimental metallic inclusions, non-metallic particulates, and dissolved gases from the metal melt using essential metallurgical techniques to enhance their chemical purity. This process is fundamental for mitigating corrosion, refining the grain structure, and eliminating structural defects (porosity, microcracks, etc.) [102]. Below these limits, impurity particles remain undetectable, thereby preventing the formation of electrochemically active cathodic sites that would otherwise intensify corrosion, leading to a marked reduction in the corrosion rate. Notably, when the Fe content in Mg alloys is maintained below 20 ppm, the corrosion resistance can approach that of aluminum alloys [103]. Furthermore, during biodegradation, Mg^{2+} released from high-purity Mg (HP Mg, $\geq$ 99.99 wt.%) can replace Ca^{2+} in hydroxyapatite (HA), forming Mg-substituted HA that enhances osteo-inductivity and osseointegration [104]. Consequently, ongoing advancements in HP Mg processing technologies are aimed at improving purification methods, with common approaches including filtration purification, electromagnetic purification, and melt self-purification [105].

2.3.1. Filtration purification

Filtration purification is fundamentally governed by three principal mechanisms including mechanical filtration, precipitation, and adsorption. Mechanical filtration restricts the passage of inclusions through the medium's pores, precipitation facilitates the deposition of fine impurities within a serrated channel, and adsorption enables the removal of residual solid or liquid contaminants [102]. For instance, Wang et al. [106] have applied this technique to a Mg-Gd-Y-Zr alloy, achieving a reduction in average inclusion size from 12.7 to 4.3 μm and a decrease in inclusion volume fraction from 0.26% to 0.06%.

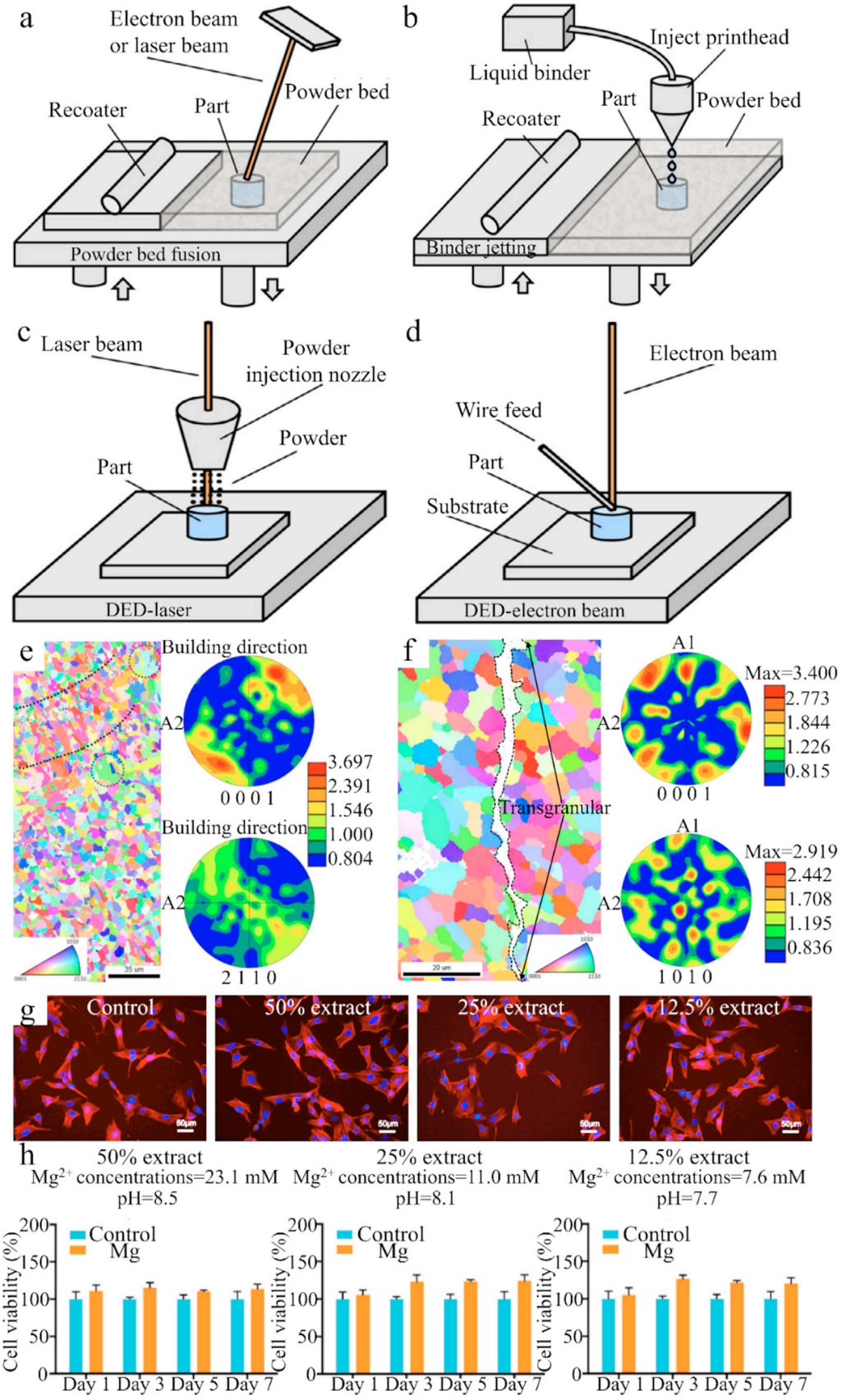

Fig. 3. Schematic of (a) powder bed fusion, (b) binder jetting, (c) laser-directed energy deposition, and (d) electron beam-directed energy deposition [84]; (e) IPF mapping of WE43 alloy (dashed line: melt line, dotted line: abnormally large grains) and PF diagram; (f) EBSD analysis of crack morphology [86]; (g) morphology of MC3T3-E1 cells and (h) viability of cells cultured in Mg-Nd-Zn-Zr extracts with varying concentrations [88]. (For interpretation of the references to color in this figure legend, the reader is referred to the web version of this article).

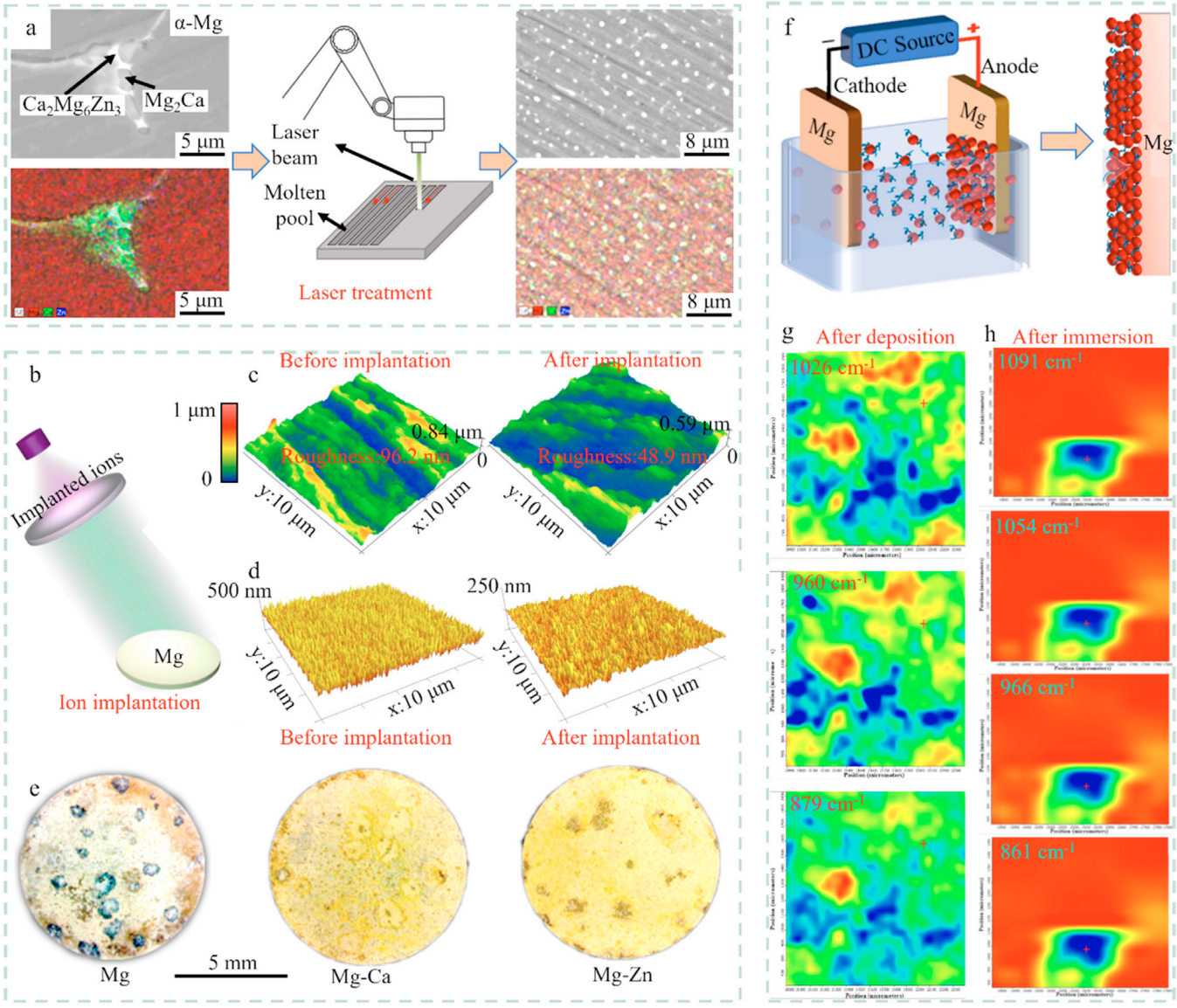

Fig. 4. (a) Microstructure images of Mg-Zn-Ca alloy before and after complete laser surface melting [121]; (b) schematic of Mn ion implantation into pure Mg and (c) atomic force microscopy images pre- and post-implantation [123]; (d) atomic force microscopy images of WE43 alloy before and after Al ion implantation [144]; (e) macroscopic morphology images of Mg, ion-implanted Mg-Ca, and ion-implanted Mg-Zn alloys after potentiodynamic polarization tests [126]; (f) schematic of EPD setup [129]; False color maps with the indicated reference bands of Fourier transform chemical spectra of coated Mg-Zn-Mn alloy before and immersion in SBF [130].

This refinement concurrently improves mechanical properties, with tensile strength increasing from 200 to 232 MPa, yield strength from 156 to 167 MPa, and elongation from 3.4% to 7.0%, while the corrosion rate declined from 38.8 to 2.5 $g{\cdot}m^{-2}{\cdot}d^{-1}$. Additionally, Le et al. [107] have evaluated the purification efficiency of AZ91 alloy under varying mesh sizes and filtration temperatures, determining that a stainless-steel mesh of 20–30 mesh per inch at 650–700 °C markedly enhances purification outcomes. Excessively high temperature intensifies oxidation, whereas overly fine meshes reduce filtration throughput, thereby establishing 650–700 °C and a 20–30 mesh sieve as the optimal processing parameters. Owing to its operational simplicity, high impurity removal efficiency, and absence of secondary contamination, filtration-based purification is frequently employed as a post-treatment step following other purification methodologies. Recent studies are increasingly focused on developing self-cleaning and reusable filtration systems to further enhance the efficacy of this technique in fabricating Mg-based biodegradable metals.

2.3.2. Electromagnetic purification

Electromagnetic purification leverages the differences in electrical conductivity between metallic and non-metallic constituents to separate inclusions from the melt via electromagnetic forces induced by an applied magnetic field. Feng et al. [108] have addressed the challenge of eliminating persistent fine inclusions in Mg alloys by employing an electric driving force, thereby achieving efficient purification. Under an applied current of 80 A, the inclusion removal rate reaches 63% within 10 min, while the pulsed current method

generates a driving force 5.5 times greater than that of static sedimentation. Li et al. [109] have investigated the effects of various electromagnetic fields on the microstructure of AZ61 alloy, finding that a static magnetic field combined with direct current completely eliminates the cellular grain boundary structure. In this configuration, Mg-Al-Zn compounds become polarized and migrate toward the melt periphery, resulting in a more uniform dispersion and a reduced overall concentration. Due to its high efficacy, contamination-free operation, and continuous processing, electromagnetic purification is often integrated with complementary techniques to enhance impurity removal during melt cooling and solidification. Recent research has increasingly emphasized the synergistic integration of electromagnetic purification with other methodologies to develop more efficient strategies for Mg melt purification, ultimately enhancing the overall quality of Mg-based biodegradable metals.

2.3.3. Melt self-purification

Melt self-purification, by avoiding the use of extraneous impurity agents, enables the segregation of elements such as Fe and Ni at the solid-liquid interface through the controlled adjustment of cooling rates and temperature gradients. This process drives impurities to accumulate at the ingot's peripheries during crystal growth, thereby facilitating effective separation. Pan et al. [110] have developed a low-temperature treatment that reduces the Fe content in AZ31 alloy from 65 to 15 ppm. Shaikh et al. [111] have applied a procedure in which the Mg ingots were melted in a stir-casting furnace at 750 °C, stirred at 650 °C for 10 min, and held for 15 min to produce Mg with 99.9% purity. Subsequent treatment with HA further refines the grain structure and reduces the biodegradation rate to 0.1 $mm \cdot y^{-1}$, thereby promoting bone formation without adverse effects. By eliminating chemical additives, this method avoids secondary contamination, thus preserving high purity. Its simplicity, cost-effectiveness, and efficiency significantly improve production outcomes. Recent research focuses on optimizing cooling rates and temperature gradients, as well as integrating supplementary purification techniques, to further enhance purification efficiency and material performance.

2.4. Surface modification

The inherently high biodegradation rate and restricted bioactivity of pure Mg substantially constrain its widespread utilization as a surgical implant material. Consequently, surface modification strategies aim at mitigating biodegradation, while enhancing biocompatibility have emerged as pivotal approaches for optimizing the performance of Mg-based implants (Table 3). For instance, laser surface treatment permits precise regulation over parameters such as power density, scanning speed, and pulse frequency to induce the formation of metastable surface architectures. This process refines the grain microstructure and mitigates galvanic corrosion, thereby reducing the corrosion rate and improving biocompatibility [112]. Similarly, ion implantation leverages the contrast in electrical conductivity between metallic and non-metallic phases by accelerating dopant ions under high voltage to produce a dense, corrosion-resistant surface layer on Mg alloys, while preserving structural homogeneity [113]. Electrochemical methods, including electrodeposition (ED), electrophoretic deposition (EPD), and micro-arc oxidation (MAO), facilitate the formation of uniform, compact coatings that markedly enhance corrosion resistance, mechanical robustness, surface hardness, and bioactivity [114]. The hydrothermal technique, prized for its cost-efficiency and simplicity, permits the deposition of organic and inorganic coatings at moderate temperatures, thereby preserving the structural integrity of Mg alloys, while augmenting their biofunctional properties [115]. Electrostatic spraying utilizes a high-voltage field to atomize a precursor solution into charged droplets, which are then electrostatically guided to form a uniform coating, making the technique particularly effective for implants with complex geometries [116]. Moreover, sol-gel-based dip coating and high-speed spin coating provide versatile methods for depositing homogeneous organic or inorganic coatings. These coatings not only reduce the biodegradation rate and enhance bioactivity but also facilitate the creation of multifunctional surfaces endowed with capabilities such as controlled drug release and antibacterial activity [117].

Despite these advances, challenges related to coating adhesion, long-term stability, and scalability persist (Table 4). To address these limitations, recent research has focused on integrating multiple surface modification techniques to further optimize the clinical performance of Mg-based biodegradable metals. To enhance coating adhesion, Li et al. [118] have employed femtosecond laser texturing to construct multiscale conical microstructures on AZ31B Mg alloy. This pretreatment significantly increases surface area and roughness, creating robust mechanical interlocking that substantially enhances the binding strength of subsequently deposited protective coatings, thereby improving long-term corrosion resistance. Chen et al. [119] have developed a PCL/Collagen/Cerium-doped HA composite coating on AZ31 Mg alloy *via* electrospinning. The intrinsic porosity and fibrous nature of the electrospun layer promotes mechanical locking with the Mg alloy substrate, while the presence of $–NH_2$ in collagen and –OH in HA enhances electrostatic interactions between the polymer coating and Mg alloy substrate, significantly reducing corrosion current density and enhancing long-term stability *in vitro*. Importantly, both femtosecond laser processing and electrospinning are highly controllable and scalable techniques. The ability to precisely adjust parameters (*e.g.*, laser fluence, pulse duration, electrospinning voltage, and flow rate) enables reproducible and standardized production, paving the way for large-scale manufacturing of advanced Mg-based implants.

2.5. Structural design

Porous, fine-grained, and composite structures represent pivotal strategies in the design of advanced materials, fundamentally modulating their chemical, physical, mechanical, and biological properties to confer tailored functionalities. Recent

Table 3
Preparation techniques and typical performance comparison of coatings on the Mg-based biodegradable metal surfaces.

Substrate	Preparation techniques	Coatings	Main findings	Ref.
Mg-Zn	Laser surface treatment	Honeycomb structure	The hardness of the alloy exhibits an increase of 24 %–27 %, and the corrosion rate demonstrates a reduction of 21 %–37 %.	[120]
Mg-Zn-Ca	Laser surface treatment	More uniform surface microstructure(Fig. 3a)	The hardness of Mg-Zn-Ca alloy increases by 24 %–27 %, and the corrosion rate is reduced by 21 %–37 %.	[121]
Mg-AZ31B	Laser surface treatment	Aplitic texture	The $Mg_{17}Al_{12}$ phase volume fraction increases to 4.2 %, the contact angle decreases to 48.5°, and the surface energy increases by 26 %.	[122]
Pure Mg	Ion implantation (Mn ion)(Fig. 4b)	Mn-O layer	The Mn ion implantation reduces the surface roughness from 96.2 to 48.9 nm (Fig. 4c).	[123]
WE43	Ion implantation (Si ion)	Si-O layer	The WE43surface becomes smoother (Fig. 4d) and the corrosion current density decreases from 642 ± 125 to 27 ± 32 $\mu A{\cdot}cm^{-2}$	[124]
Mg-1Ca	Ion implantation (Y ion)	Y-O layer	The corrosion rate decreases from 2.10 ± 0.21 to 0.69 ± 0.18 $mm{\cdot}y^{-1}$.	[125]
Pure Mg	Ion implantation (Ca ion)	Ca-rich layer	The corrosion current density of Ca-implanted Mg decreases to 100 $\mu A{\cdot}cm^{-2}$, exhibiting the least localized biodegradation (Fig. 4e).	[126]
Mg-Zn-Ca	ED	Ca-deficient HA coating	The corrosion potential increases from −1645 to −1414 mV, and the corrosion current density decreases from 110 to 25 $\mu A{\cdot}cm^{-2}$.	[127]
ZE21B	ED	MTA/$Mg(OH)_2$ coating	The coating significantly inhibits the adsorption of plasma fibrin and activation of platelets, and reduces the hemolysis rate to 0.97 ± 0.18 %.	[128]
Mg-Ca	EPD(Fig. 4f)	Alginate/bioglass composite coating	The corrosion current density decreases by 51.3 % to 23.1 $\mu A{\cdot}cm^{-2}$.	[129]
Mg-Zn-Mn	EPD	HA coating	The coating composition is homogeneous before and after immersion in the simulated body fluid (SBF) (Fig. 4g and h)	[130]
AZ31B	MAO	Zn-doped phosphate coating	The weight loss of the coated sample in SBF for 56 days is only 5.22 %.	[131]
ZK60	Hydrothermal treatment	Sr-doped HA coating	The corrosion current density decreases from 5.09×10^{-6} to 1.65×10^{-6} $A{\cdot}cm^{-2}$, and Sr promotes cell adhesion and proliferation.	[132]
AZ31	Hydrothermal treatment	Zn-supported montmorillonite coating	The coating reduces the corrosion current density of AZ31 alloy from 2.8×10^{-5} to 2.8×10^{-7} A cm^{-2}.	[133]
AZ31	Hydrothermal treatment	HA and ZnO double-layer nanoarray coating	The bactericidal rates against *Staphylococcus aureus* and *Escherichia coli* are 96.5 % and 94.3 %, respectively.	[134]
ZE21B	Electrostatic spraying	Schiff base/NP@S-HA composite coating	The composite coating confers superior overall properties to the Mg alloy, including reduced corrosion, enhanced cell proliferation and migration, and strong anti-inflammatory function.	[116]
Pure Mg	Dip coating	Polyurethane polymer coating	The corrosion current density decreases from 353.8 ± 14.5 to 1.422 ± 0.07 $\mu A{\cdot}cm^{-2}$.	[135]
AZ31 and Mg4Y	Dip coating	PLGA coating	The biocompatibility of the coated sample is better than that of AZ31 and Mg4Y alloys.	[136]
Mg-Nd-Zn-Zr	Dip coating	Polydopamine (PDA)/Cu(II) coating	The coating achieves continuous release of copper ions, promotes the growth of endothelial cells, and inhibits the proliferation of smooth muscle cells.	[137]
Mg-2Zn	Chemical conversion coating	Mg-phenol network	The coating significantly promotes the adhesion and proliferation of rat BMSCs.	[138]
AZ31	Dip coating	Chitosan/polylactic acid (PLA) composite coating	The PLA seals the pores of the chitosan layer, and the corrosion current density of AZ31 alloy is reduced by 4 orders of magnitude.	[139]
AZ31B	Dip coating	Ce_xO_y/SiO_2 coatings	The coating retards the degradation rate after immersion in SBF for 21 days.	[140]
AZ91D	Sol-gel method	Silicon-based coating	The corrosion current density drops from 6.23 to 0.15 $\mu A{\cdot}cm^{-2}$.	[141]
WE43	Spin coating	Hyaluronic acid and branched polyvinylidene double-layer coating	The coating has a fast and cyclic self-healing ability that restores the original structure and function.	[142]
Mg-1Ca	Spin coating	Silk protein-HNT/PA coating	The coatings respond quickly and self-repair effectively, thereby significantly improving corrosion resistance.	[143]

advances have exploited these structural modifications to optimize biodegradation kinetics, mechanical stability, and biocompatibility of Mg-based biodegradable metals. Specifically, porous structures enable the modulation of biodegradation rates and promote cell adhesion and proliferation, primarily through adjustments in porosity. Fine-grained microstructures, achieved through grain refinement and an increased density of grain boundaries retard biodegradation rates, while enhancing mechanical performance. Meanwhile, composite materials, integrating biodegradable Mg alloys with polymers or ceramics,

Table 4
Advantages and disadvantages of preparation techniques for coatings on the Mg-based biodegradable metal surfaces.

Preparation techniques	Advantages	Disadvantages
Laser surface treatment	Precise control of surface properties	Induction of heat-affected zones
Ion implantation	Enhanced corrosion resistance and increased surface hardness	Introduction of residual internal stresses
Electrochemical treatment	Cost-effectiveness and uniform coating deposition	Insufficient coating adhesion
Hydrothermal method	Formation of dense coatings and enhanced biocompatibility	Prolonged reaction times and solution composition sensitivity
Dip coating	Operational simplicity and scalability for large-area applications	Variability in coating thickness
Spin coating	Superior uniformity for coating	Limited applicability to small sample

synergistically reduce biodegradation kinetics, improve mechanical strength, and enhance biocompatibility by leveraging complementary material properties. Collectively, these strategies underscore the potential of structural design to overcome the intrinsic limitations of Mg-based implants for clinical applicability.

2.5.1. Porous structures

Porous scaffolds are integral to bone tissue engineering, utilizing interconnected pore networks to promote *in vivo* tissue ingrowth, cell proliferation, and osteogenic differentiation. Dong et al. [145] have demonstrated that Mg-Zn scaffolds exhibit a significant reduction in corrosion rate (from 2.3 ± 0.9 mm·y^{-1} to 0.7 ± 0.1 mm·y^{-1}) and maintain their structural integrity after soaking in SBF for 28 days (Fig. 5a). Concurrently, their yield strength and Young's modulus remain within the range of trabecular bone, and extracts show favorable cytocompatibility with MC3T3-E1 pre-osteoblasts. Wang et al. [146] have revealed superior compressive strength and stiffness in WE43 Mg alloy scaffolds with 500 μm-diameter pores (P500) (Fig. 5b-c). Biodegradation products accumulate predominantly in the scaffold's central region (Fig. 5d) and the scaffolds support osteogenic differentiation (Fig. 5e and f).

Crucially, the overall porosity profoundly dictates both mechanical integrity and degradation kinetics. Rezaei-Baravati et al. [147] have found that Mg-3Al-1Zn-0.5Ca alloy scaffolds with 30% porosity exhibit superior compressive strength (72 MPa) and a slower corrosion rate (3.5 mm·y^{-1}) compared to those with 50% porosity (21 MPa and 4.3 mm·y^{-1}, respectively). This is attributed to the larger load-bearing solid volume and reduced specific surface area at lower porosities, which limits exposure to corrosive environments and enhances structural robustness. Saad et al. [148] have demonstrated that increased porosity directly accelerates degradation rates, consequently impairing porous Mg scaffold structural properties and fracture resistance. This highlights a critical design trade-off: while higher porosity enhances cellular infiltration and nutrient transport, it simultaneously accelerates material loss, potentially compromising mechanical support during bone healing. Although the mechanical properties of porous Mg scaffolds during early-stage implantation (*e.g.*, compressive strength: 0.2–80 MPa, Young's modulus: 0.01–2 GPa) remain comparable to those of native bone [149], their inherently large surface area and enhanced fluid dynamics accelerate corrosion. To mitigate this, coating processes are commonly employed to optimize performance. For example, Kang et al. [150] have engineered porous Mg scaffolds that mimicking natural bone architecture and applied an HA/(PEI-SiO_2) coating to significantly reduce corrosion rate and improve osteogenesis *in vivo* (Fig. 5g).

2.5.2. Fine-grained structures

Fine-grained structures enhance the corrosion resistance of Mg-based materials by increasing the density of grain boundaries, which mitigates the interfacial mismatch between the oxide layer and Mg substrate, thereby minimizing the formation of oxide cracks. Qu et al. [151] have reported that finer grain structures in pure Mg correlate with slower biodegradation rate owing to reduced biodegradation kinetics. Hofstetter et al. [152] have engineered ZX10 alloy to achieve a 2 μm grain size, resulting in high strength, excellent ductility, and reduced mechanical anisotropy, and uniform, gradual biodegradation without hydrogen accumulation.

Roche et al. [153] found that smaller microstructure sizes increased the corrosion potential to nobler values and decreased the corrosion current densities for Mg-Zn-Ca crystalline alloys.

Similarly, Ge et al. [154] have employed equal channel angular pressing (ECAP) on ZM21 alloy, refining its grains to 500 nm and enhancing its yield strength from 180 to 340 MPa, while maintaining ductility. However, excessive grain refinement may impair plasticity and destabilize the biodegradation behavior. To address these challenges, composite structures that integrate Mg-based materials with ceramics or polymers have emerged as a versatile strategy, offering enhanced mechanical performance and corrosion resistance, while enabling the tuning of biodegradation kinetics to meet diverse clinical requirements.

2.5.3. Composite structures

Composite structure design has emerged as a widely adopted and effective strategy to achieve integrated performance enhancement and functional optimization in Mg-based biodegradable metals. In these composites, the performance is determined by the content, spatial distribution, and particle size of the reinforcing phases. Phosphate-based bioceramics such as HA and beta-tricalcium phosphate (β-TCP) are commonly employed as reinforcing materials in Mg-based biodegradable metals due to their excellent biocompatibility [155].

HA, renowned for its favorable bioactivity and corrosion resistance, serves as an effective reinforcing phase in Mg-based composites, despite its limited load-bearing capacity

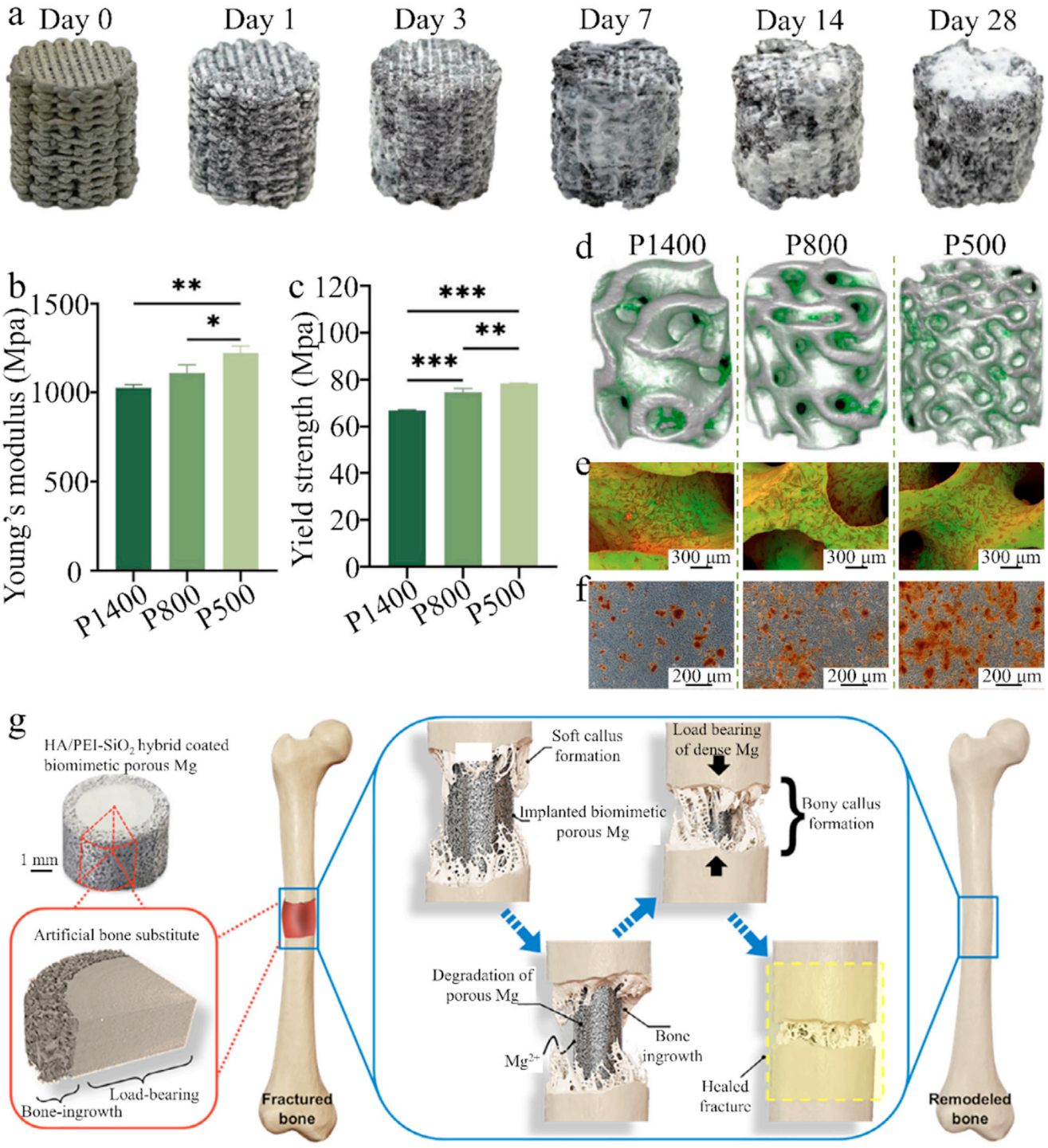

Fig. 5. (a) Visual inspection of Mg-Zn scaffold degradation during immersion in SBF over time [145]; (b) Young's modulus, (c) compressive strength, (d) three-dimensional reconstructed micro-CT images of biodegradation products, (e) morphology of BMSCs, and (f) images after alizarin red staining of Mg alloy scaffolds with different pore sizes [146]; (g) structural design of biomimetic porous Mg, where porous Mg features a dense core surrounded by a porous outer layer as an artificial bone substitute, along with a schematic of the fracture healing process and biodegradation of the biomimetic porous Mg scaffold [150]. (For interpretation of the references to color in this figure legend, the reader is referred to the web version of this article).

[156]. Jaiswal et al. [157] have found that cylindrical HA reinforcement increases compressive strength of Mg-3Zn by 40% compared to spherical HA reinforcement (Fig. 6a and b), despite both types fracturing into two distinct segments. This strength enhancement is attributed to the Hall-Petch strengthening mechanism, which enhances resistance to plastic deformation by impeding dislocation movement and promoting grain refinement [158]. Moreover, Mehdizade et al. have employed friction stir processing (FSP) to achieve a uniform dispersion of the HA nanoparticles in the WE43 alloy ma-

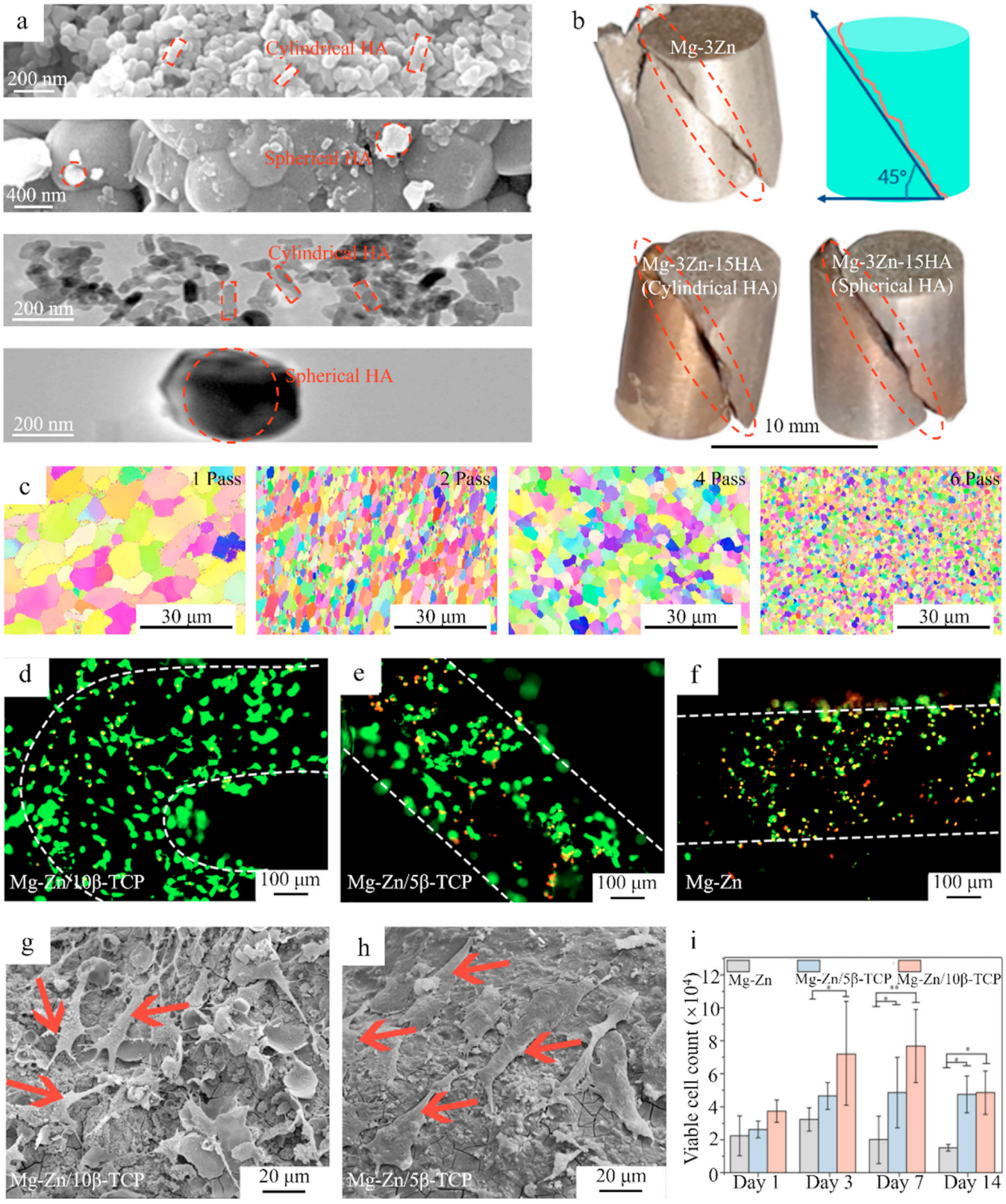

Fig. 6. (a) SEM and transmission electron microscopy images of cylindrical and spherical HA, (b) macroscopic images of Mg-3Zn/HA composite after uniaxial compression testing [157]; (c) EBSD images of Mg-HA composite after FSP treatment [167]; *In vitro* biological evaluation of Mg-Zn/5β-TCP and Mg-Zn/10β-TCP after incubation for 3 days: fluorescence staining images of MC3T3-E1 pre-osteoblasts on (d) Mg-Zn/10β-TCP, (e) Mg-Zn/5β-TCP, and (f) Mg-Zn (white dashed lines indicate rough edges of scaffold struts); morphology of pre-osteoblasts (red arrows) cultured on (g) Mg-Zn/10β-TCP and (h) Mg-Zn/5β-TCP, and (i) number of surviving pre-osteoblast nuclei [162]. (For interpretation of the references to color in this figure legend, the reader is referred to the web version of this article).

trix (Fig. 6c). This technique elevates the yield strength to 226 MPa, while significantly reducing the biodegradation rate. This strength improvement and retarded degradation result from nano-HA particles acting as effective dislocation barriers and contributing to the formation of a more compact and stable passive layer, respectively [159]. Specifically, Ca^{2+} and PO_4^{3-} reach local supersaturation in the physiological environment, which promotes heterogeneous nucleation and precipitation of amorphous calcium phosphate and HA on the Mg alloy surface, forming a dense, bioactive coating that acts as a physical barrier [160].

β-TCP is widely utilized owing to its recognized bioactivity and osteo-conductivity [161]. Its release of Ca^{2+} and PO_4^{3-} ions in physiological fluids can promote the formation of a protective calcium phosphate layer, thereby mitigating corrosion. Dong et al. [162] have developed Mg-Zn/β-TCP scaffolds using additive manufacturing, achieving a controlled biodegradation rate of 0.5 $mm{\cdot}y^{-1}$ along with enhanced cell adhesion and proliferation. Spindle-shaped pre-osteoblasts adhere to both the Mg-Zn/5β-TCP (Fig. 6e) and Mg-Zn/10β-TCP (Fig. 6d) scaffolds, whereas predominantly rounded, red-stained cells are observed on the unreinforced Mg-Zn scaffold (Fig. 6f), further confirmed by SEM analysis (Fig. 6g-i). These benefits are primarily attributed to Ca^{2+} released during β-TCP degradation, which directly participate in cellular signaling pathways, induce osteoblast differentiation, and promotes extracellular matrix mineralization, thereby creating a more favorable microenvironment for osseointegration [163]. Additionally, He et al. [164] have incorporated nano-sized β-TCP particles in Mg-3Zn-0.8Zr alloy, demonstrating that the resulting composite exhibits markedly superior corrosion resistance compared to the unreinforced alloy.

3. Status of animal experiments and clinical application research on Mg alloys

In addition to *in vitro* assessments, *in vivo* investigations are essential for validating the safety and efficacy of high-risk medical device candidates prior to clinical trials [165]. Biological safety evaluations are typically conducted using small animal models such as mice, rats, or rabbits in accordance with ISO standards. These evaluations include a range of standardized assays such as irritation and skin sensitization tests, systemic toxicity studies, local implantation analyses, and pharmacokinetic assessments, which are designed to systematically identify potential health risks to patients [166]. For evaluating biological efficacy, large animal models such as sheep, goats, pigs, monkeys, or dogs are employed in indication-specific studies to assess the therapeutic efficacy of novel Mg-based devices against established benchmarks. Despite the physiological similarities among mammalian species, significant differences between small animals, large animals, and humans must be considered. For instance, variations in skeletal dimensions and load-bearing conditions across species can influence the required mass and in-service mechanical environment of Mg-based implants undergoing biodegradation or absorption, potentially leading to discrepancies between preclinical outcomes and clinical performance. Consequently, systematic comparative studies focusing on the clinical translation of Mg alloy materials in orthopedic, dental, and vascular applications should be a key focus in the future research and development of Mg-based medical devices. Fig. 7 presents a timeline summarizing the progression of Mg alloy development from animal experiments to clinical translation. Building on these essential preclinical assessments, Mg-based biodegradable metals now demonstrate significant potential across multiple clinical applications, including orthopedic implants, vascular intervention devices, and GBR membranes.

3.1. Orthopedic implants

Mg-based biomedical metals are poised to be central to the development of biodegradable orthopedic devices. During active biodegradation via a rapid ionization process, these implants contribute to the healing of surrounding hard tissues, while surplus Mg is efficiently cleared via renal metabolism. Their elastic modulus closely approximates that of human bone, thereby facilitating natural load transfer, stimulating bone remodeling, and mitigating stress shielding that is a limitation commonly associated with conventional metallic implants. To date, more than 20 Mg-based biodegradable alloys have been systematically evaluated for bone repair in preclinical models, spanning both small animal species (*e.g.*, rats, rabbits, guinea pigs) and large animal models (*e.g.*, sheep) [184]. For example, Lee et al. [168] have assessed the performance of Mg-5Ca-1Zn alloy in New Zealand rabbits. Energy-dispersive X-ray (EDX) analysis demonstrates a gradual attenuation of Mg and O peak intensities with increasing distance from the implant surface (Fig. 8b). Over time, the interface between the Mg alloy and bone migrated toward the implant center, with displacement reaching approximately 15% at 8 weeks, 30% at 16 weeks, and 45% at 24 weeks (Fig. 8c). Antoniac et al. [169] have implanted Mg-1Ca alloy into rabbit bone and muscle tissues (Fig. 8d), with histological evaluation confirming its biodegradation occurred without local toxicity, and showing that surrounding tissues maintained morphology comparable to controls. Similarly, Li et al. [49] have implanted Mg-2Zn-1Mn alloy into rat femora, with pathological assessments revealing no evidence of cytotoxicity or systemic toxicity in the rats (Fig. 8e). Further, alkaline phosphatase (ALP) and alizarin red staining indicate enhanced tissue regeneration and Ca nodule formation over time (Fig. 8f), while increased expression of osteogenic marker proteins underscores the promotion of osteogenic differentiation by the Mg-2Zn-1Mn implant (Fig. 8g).

In the clinical translation arena, pure Mg, Mg-Y-RE-Zr alloy, and Mg-Ca-Zn alloy have attained regulatory approval for orthopedic applications in China, Germany, and South Korea, respectively. In China, Zhao et al. [170] have evaluated biodegradable pure Mg screws in patients with femoral head necrosis. At 12 months post-implantation, the screw diameter decreased by approximately 25%, with no signs of screw deformation or pericapsular tissue necrosis, and serum levels of

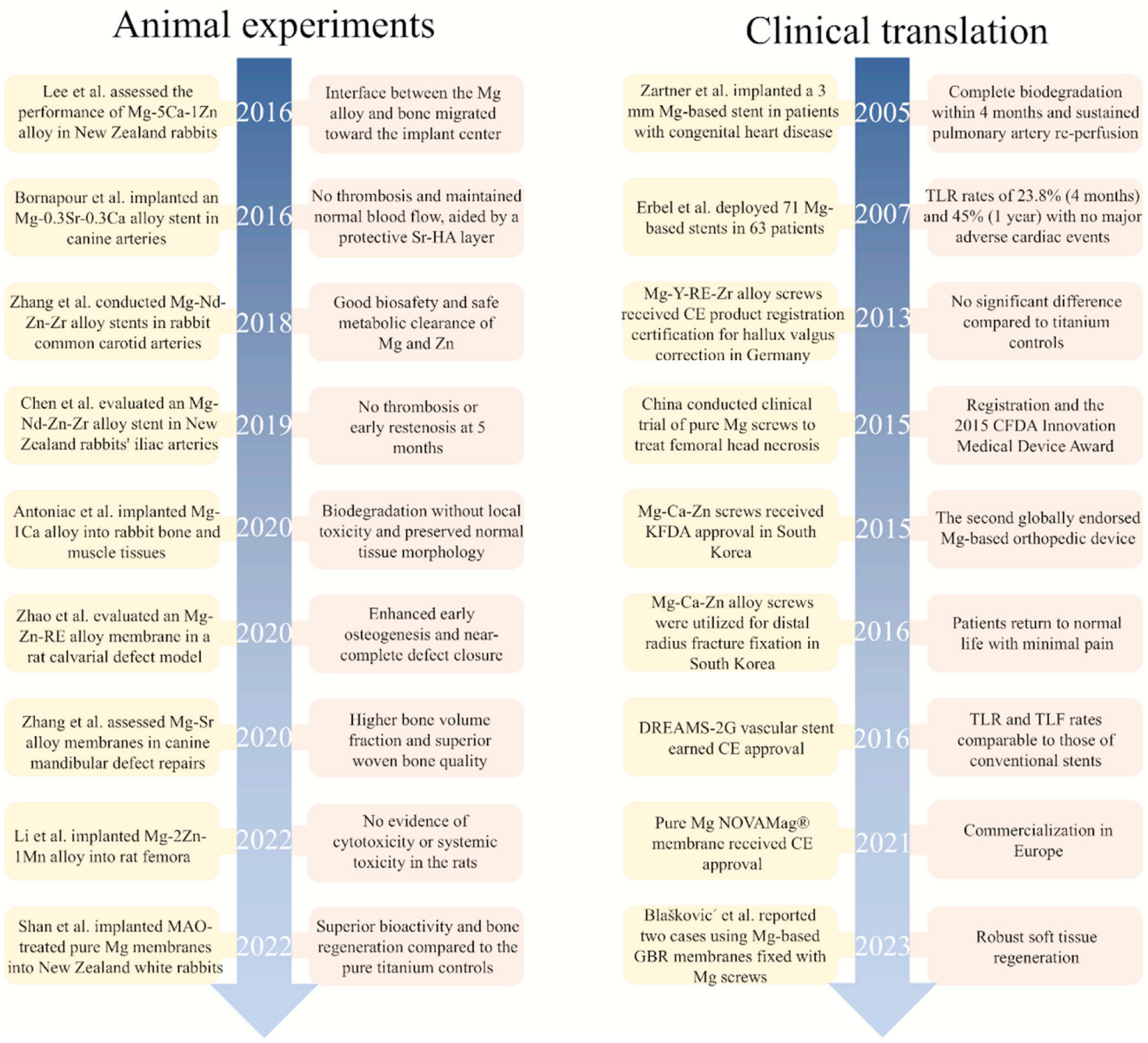

Fig. 7. Timeline of animal studies and clinical research on Mg alloys for orthopedic implants [49,168–171], vascular intervention devices [172–178], and GBR membranes [179–183].

Ca, Mg, and P remain within normal limits. This landmark study, the first clinical trial of its kind in China, facilitated the registration process of pure Mg screws, culminating in the 2015 China Food and Drug Administration (CFDA) Innovation Medical Device Award [171]. In Germany, Mg-Y-RE-Zr alloy screws have been used for hallux valgus correction, and 6-month follow-up data shows no significant differences in hallux pain or metatarsophalangeal (MTP) joint range of motion compared to the titanium control group, and these screws received CE product registration certification in 2013 [171]. Furthermore, in South Korea, Mg-Ca-Zn alloy screws have been utilized for distal radius fracture fixation (Fig. 8a) [168]. Follow-up assessments after 6 and 12 months reveal that 53 patients achieve return to normal life, reporting minimal pain (visual analog scale: 1.38 ± 1.1), normal joint mobility and grip strength, and a Disabilities of the Arm, Shoulder, and Hand (DASH) score of 29.82 ± 4.4. This study supported the approval of Mg-Ca-Zn screws by the South Korean Food and Drug Administration (KFDA) in 2015, marking the second globally endorsed Mg-based orthopedic device and advancing the clinical translation of novel Mg implants. This progress has significantly encouraged clinicians and scientists to accelerate the translation of new Mg implants designed for emerging indications.

3.2. Vascular intervention materials

Design criteria for vascular stents primarily encompass mechanical performance, controlled biodegradation, and vascular biocompatibility. Mechanically, these stents must resist elastic

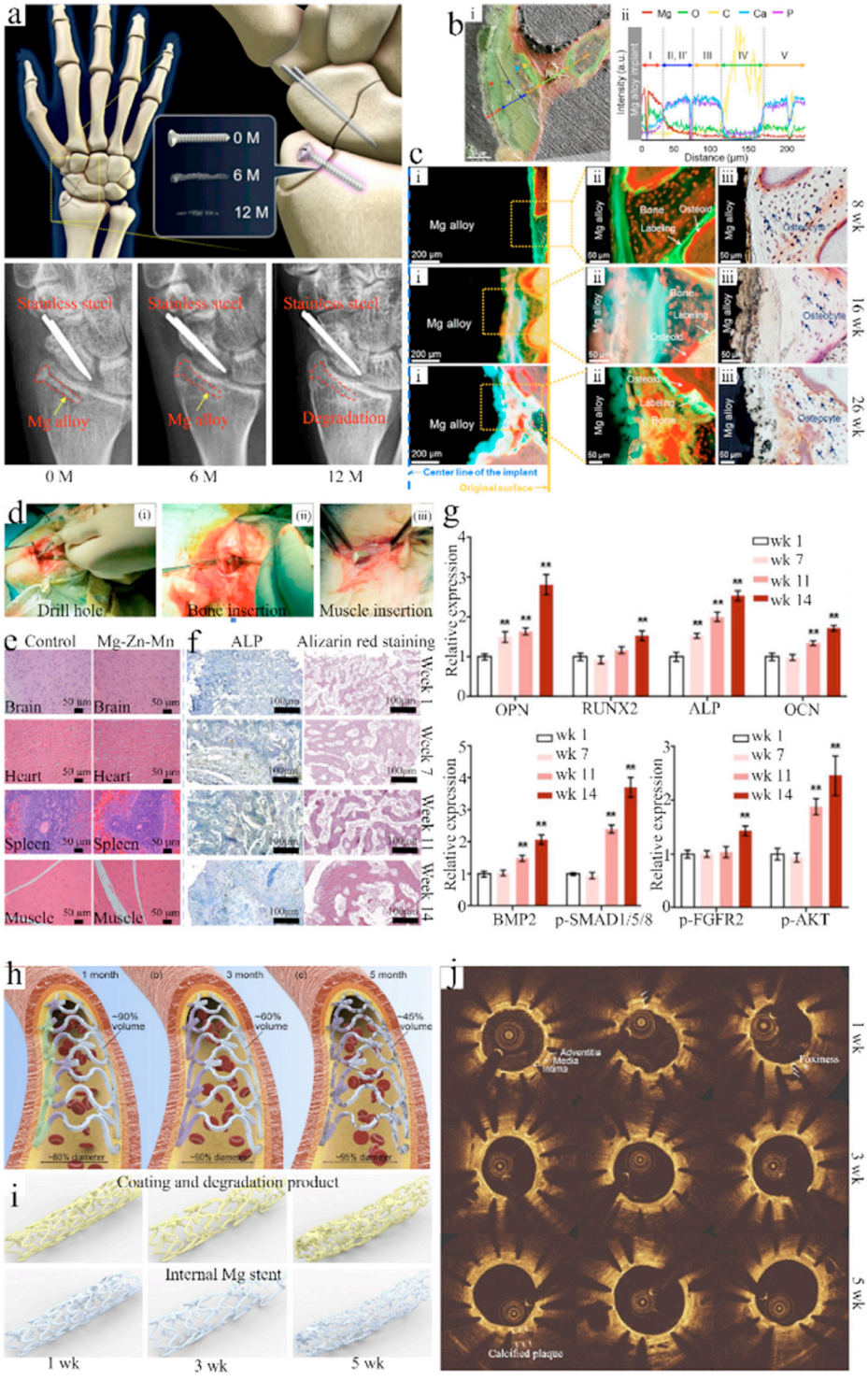

Fig. 8. (a) Clinical observation of complete biodegradation of Mg alloy screws and bone healing process over 12 months; (b) separation of Mg alloy-implant interface region: (i) merged fluorescence and SEM images and (ii) SEM/EDX line profiles; (c) gradual biodegradation of Mg alloy interface after implantation, with bone formation by staining in Villanueva stain: (i) Mg alloy biodegradation observed under low-magnification fluorescence, (ii) bone formation observed under high-magnification fluorescence, and (iii) bone formation observed under high-magnification natural light [168]; (d) surgical procedure steps: (i) drilling, (ii) bone graft insertion, and (iii) muscle insertion [169]; (e) histopathological images of various rat organ specimens after implantation with Mg-2Zn-1Mn alloy for 16 weeks; (f) tissue and Ca nodule formation determined by ALP and alizarin red staining after implantation with Mg-2Zn-1Mn alloy for 1, 7, 11, and 14 weeks; (g) protein levels of BMP-2, p-SMAD1/5/8, β-actin, p-FGFR2, and p-AKT measured by Western blot ($^{**}P < 0.01$) [49]; (h) schematic of postoperative stent changes over time; (i) 3D models reconstructed by high-resolution micro-CT of coated OPT stents after post-implantation for 1, 3, and 5 months; (j) *in vivo* observation by optical coherence tomography [172]. (For interpretation of the references to color in this figure legend, the reader is referred to the web version of this article).

recoil and post-expansion shrinkage, while maintaining structural integrity for 3–6 months to ensure vessel patency. Furthermore, the stent surface should promote endothelial cell adhesion and concurrently suppress excessive intimal hyperplasia to avert restenosis. From a biodegradation perspective, an optimal biodegradation rate should not exceed 0.02 $mm \cdot y^{-1}$, with complete biodegradation occurring within 12–24 months to enable timely vessel remodeling. Biocompatibility mandates that the implant does not induce toxicity or adverse inflammatory responses, and that its biodegradation products are harmless [185].

Chen et al. [172] have evaluated an Mg-Nd-Zn-Zr alloy stent with an optimized coating implanted into the iliac arteries of New Zealand white rabbits. Micro-CT and optical coherence tomography (OCT) analyses at 5 months confirm no signs of thrombosis or early restenosis, demonstrating that the stent effectively supports the vessel before biodegradation and allows for arterial healing afterwards (Fig. 8h-j). Zhang et al. [173] have conducted a 20-month study of Mg-Nd-Zn-Zr alloy stents implanted in rabbit common carotid arteries, demonstrating good biosafety. Metabolic clearance of the Mg and Zn elements is confirmed to be safe, with no accumulation of the Nd or Zr elements in vital organs. The volume of biodegradation products and Ca concentrations diminish over the long term, mitigating the risk of vascular calcification. Bornapour et al. [174] have implanted an Mg-0.3Sr-0.3Ca alloy stent in canine arteries for 5 weeks, noting the absence of thrombosis and maintenance of normal blood flow. The development of a protective Sr-HA layer on the stent surface significantly enhances the alloy's stability.

To date, Mg-based biodegradable metals constitute the largest number of studies related to the clinical translation of cardiovascular stents. Erbel et al. [175] have deployed 71 Mg-based stents in 63 patients, reporting a target lesion revascularization (TLR) rate of 23.8% after implantation for 4 months, rising to 45% at 1 year, with no occurrences of myocardial infarction, thrombosis, or mortality. Angiographic evaluation at 4 months reveals a 48.4% increase in stenosis diameter, while intravascular ultrasound (IVUS) detects minimal residual stent material integrated into the intima. Zartner et al. [176] have implanted a 3 mm Mg-based biodegradable stent in patients with congenital heart disease, achieving complete biodegradation within 4 months and sustained left pulmonary artery re-perfusion. Among Mg-based stents, the Drug-Eluting Absorbable Metal Scaffold (DREAMS) series stands out. The BIOSOLVE-I trial validates the safety of the DREAMS stent [177], while the BIOSOLVE-II trial demonstrates that the DREAMS-2 G variant achieves TLR and target lesion failure (TLF) rates comparable to conventional stents after implantation for 6–12 months, earning CE approval in 2016 [178]. Garcia et al. [186] have found that the DREAMS-2 G restores vascular geometry and completes biological absorption within 12 months. Haude et al. [187] have reported a six-month study of DREAMS-3 G stents in 116 patients, observing a late lumen loss of 0.21 mm, representing a 52% improvement compared to DREAMS-2 G. IVUS confirms stable stent dimensions and minimal neointimal formation, positioning DREAMS-3 G as a promising alternative to permanent metallic implants.

3.3. Guided bone regeneration membranes

Guided bone regeneration (GBR) membranes serve as barrier materials, isolating bone defect sites from surrounding soft tissues to prevent the infiltration of epithelial and fibroblast cells into the regenerative zone. This occlusion allows sufficient time for stem cells and osteoblasts to repair and regenerate bone tissue *in situ*. An ideal GBR membrane must exhibit excellent biocompatibility to avoid detrimental effects on surrounding tissues during the healing process. For resorbable variants, the membrane should degrade autonomously or integrate seamlessly with the host tissue. Additionally, it must possess adequate mechanical strength and dimensional stability to resist collapse within the defect, thereby preserving space for osteogenesis. The membrane should balance its occlusive properties, preventing unwanted cell migration while permitting oxygen and nutrient diffusion, with clinical manageability, avoiding excessive rigidity that could compromise adjacent tissues or induce soft tissue dehiscence. Last, superior bioactivity is essential to enhance bone tissue proliferation and differentiation [188].

Mg-based biodegradable GBR membranes have emerged as promising alternatives to traditional materials, such as collagen membranes and titanium meshes, due to their enhanced mechanical properties, biodegradability, biocompatibility, and osteogenic potential. Upon implantation, these membranes effectively segregate regenerating bone from rapidly proliferating soft tissues, fulfilling both barrier and space-maintenance roles in the initial healing phase. As Mg degrades, the released Mg^{2+} stimulates osteoblast proliferation and differentiation, while the formation of a surface oxide layer moderates further corrosion. Over time, the membrane is gradually supplanted by healthy tissue [189]. This dynamic biodegradation profile positions Mg-based GBR membranes as particularly beneficial for addressing oral and maxillofacial bone deficiencies, including alveolar bone defects and peri–implant bone loss.

Preclinical studies have confirmed the efficacy and safety of Mg-based GBR membranes. Shan et al. [179] have implanted MAO-treated pure Mg membranes into New Zealand white rabbits, reporting no infection or mortality within 3-day post-implantation. At 2 weeks, the MAO-Mg membranes demonstrate superior bioactivity and bone regeneration compared to the pure titanium controls, and both materials exhibit comparable osteogenic outcomes after 8 weeks. Zhao et al. [180] have evaluated an Mg-Zn-RE alloy membrane (6 wt.% Zn, 2.7 wt.% rare earth elements) in a rat calvarial defect model, observing enhanced early osteogenesis and near-complete defect closure by 8 weeks. Zhang et al. [181] have compared Mg-Sr alloy membranes to mineralized collagen membranes in canine mandibular defect repairs, with the Mg-Sr group showing a significantly higher bone volume fraction and superior woven bone quality, indicative of enhanced regenerative capacity.

In clinical settings, Mg-based biodegradable GBR membranes have shown significant promise, particularly in dentistry. Since receiving CE approval in 2021, the pure Mg NOVAMag® membrane (botiss biomaterials GmbH, Germany) has been commercialized across Europe [182]. Elad et al. [190] have pioneered its use for reconstructing buccal or palatal walls of extraction sockets, with 4-month follow-up data confirming satisfactory bone regeneration and soft tissue healing across all cases. Blaškovic' et al. [183] have reported that two cases of Mg-based GBR membranes secured with Mg screws show robust soft tissue regeneration at 3 months, with no evidence of membrane exposure or material leakage.

To advance the clinical translation of Mg-based biodegradable metals, material innovation is imperative. Future work should focus on developing advanced alloys with controlled degradation, optimized mechanical properties, and enhanced long-term biocompatibility to ensure predictable *in vivo* performance and overcome the translational gap of Mg-based GBR membranes.

4. New technologies and breakthroughs from biomedical Mg raw materials to biomedical device products

Achieving integrated innovation across the entire production chain from biomedical-grade Mg raw materials to biomedical devices is crucial for facilitating the clinical translation and implementation of Mg-based biodegradable metals in healthcare. In recent years, the authors' group has addressed the specific requirements of Mg-based medical devices, realizing significant technological progress in biomedical HP Mg and its alloy materials. By integrating design, research and development (R&D), production, and evaluation into a unified workflow, the authors have established a patented, end-to-end processing technology and standardized protocol for HP Mg (99.99%) raw materials, representative medical device prototypes, and their associated protective coatings. The key contributions encompass three domains as follows.

(1) Development of HP Mg raw materials: The authors have developed seven distinct series of industrial-grade HP Mg products, including ingots, wires, plates, strips, and fine-diameter thin-walled tubes, etc. These materials demonstrate superior specific strength, a low elastic modulus, and broad applicability, with mechanical properties exceeding those of conventional Mg alloys. By employing proprietary Mg metal toughening regulation technology and an advanced design framework, the authors' group has also developed novel Mg-Zn alloys and composite materials optimized for biomedical applications.
(2) Advanced protective coatings: The authors have designed two advanced categories of multifunctional, durable coatings including physical barrier coatings and self-healing coatings for the surface protection of HP Mg and its alloys. These include four polymer-based, five ceramic-based, and one self-healing coatings, which demonstrate excellent biocompatibility and precisely controlled biodegradation kinetics. These coatings significantly enhance corrosion resistance and prolong the functional lifespan of Mg-based implants.
(3) Medical device applications: The HP Mg materials have been effectively integrated into five distinct categories of bone screws for the restoration of various bone injuries and defects. Additionally, the authors have developed a novel WAAM technology, yielding printed Mg alloy medical devices with performance metrics such as tensile strength and biodegradation behavior comparable to those of conventionally cast and forged counterparts.

These advancements have been disseminated via a series of review articles in the Journal of Magnesium and Alloys, a leading international publication in the field of metallic materials, culminating in the 2023 Journal of Magnesium and Alloys Contribution Award. This recognition underscores the importance of the integrated approach in advancing Mg-based biodegradable medical devices toward clinical translation.

4.1. Processing of biomedical Mg raw materials

4.1.1. Strength and toughness enhancement design methods and processing techniques for HP Mg raw materials

Although Mg demonstrates promising attributes including *in vivo* biodegradation, its excessively rapid initial biodegradation undermines mechanical integrity, thereby significantly limiting its clinical applicability. Alloying remains a widely employed strategy to modulate Mg biodegradation kinetics. However, the addition of specific alloying elements can trigger galvanic corrosion, resulting in heterogeneous biodegradation patterns. Such uneven corrosion exacerbates stress concentrations, potentially impairing structural stability and may introduce cytotoxic risks owing to the release of toxic ions. HP Mg, free from alloying constituents, provides enhanced biodegradation and biocompatibility. However, its limited strength and propensity for deformation under load render it unsuitable for load-bearing biomedical applications. Grain refinement coupled with the introduction of stacking faults (SFs) into the hexagonal close-packed (HCP) crystal lattice to hinder dislocation motion represents well-established approaches to improve strength of pure Mg. Nevertheless, the high stacking fault energy of Mg poses considerable challenges for introducing SFs in HP Mg.

To address the intrinsic limitations of HP Mg, namely insufficient strength and toughness, suboptimal room-temperature formability, and pronounced springback, which hinder its biomedical and industrial applications, the authors' group has developed an innovative, cost-effective processing technique that integrates warm extrusion with room-temperature rotary swaging (the Chinese Invention Patent number is ZL202210243188.7). This method subjects HP Mg to uniform plastic deformation under triaxial compressive stress at moderate (100–300 °C) and ambient temperatures, utilizing a small-strain-per-pass approach that accumulates large deformations. Fig. 9a-b show that although the

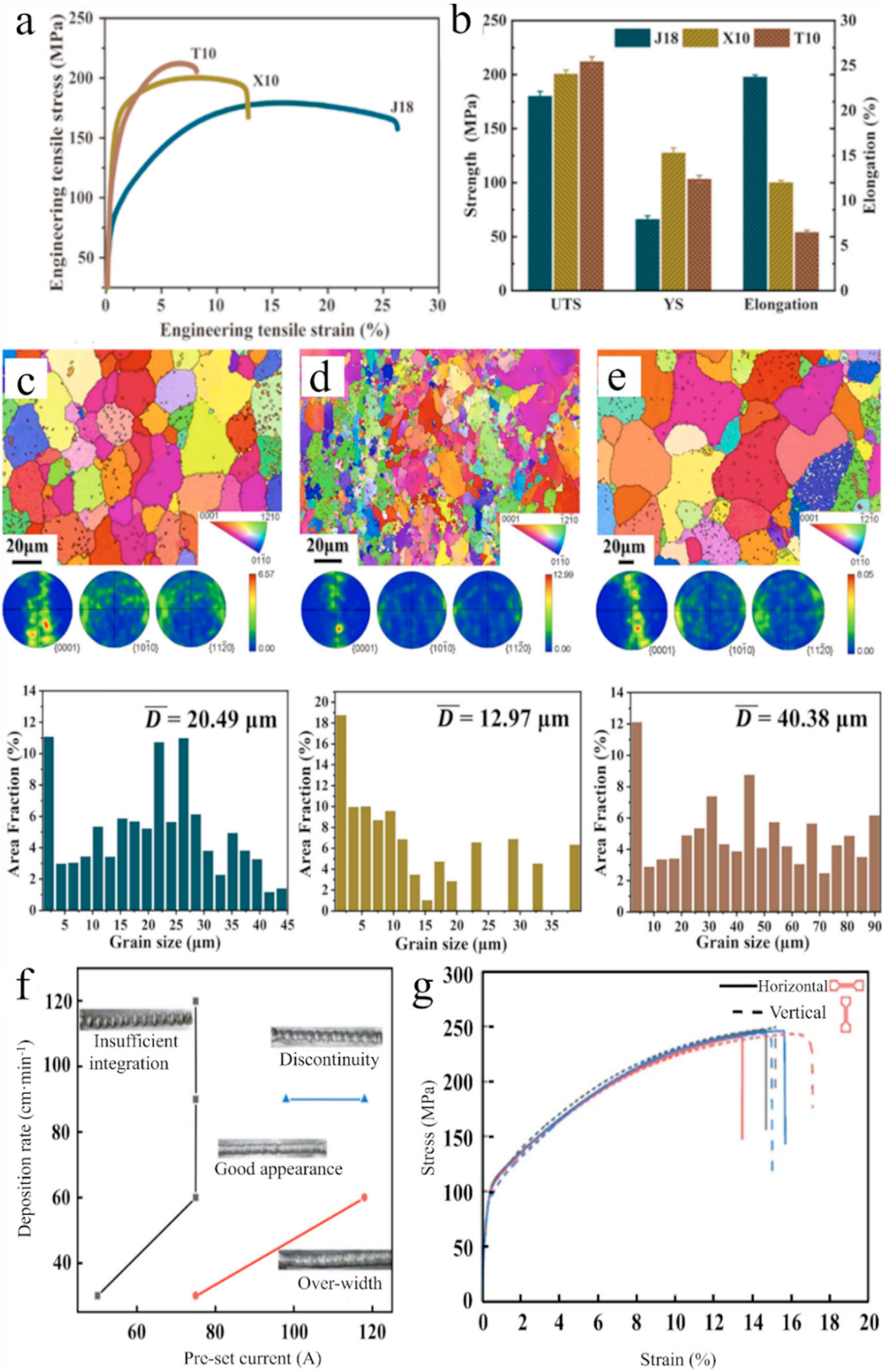

Fig. 9. (a) Tensile curve, (b) ultimate tensile strength, yield strength, and elongation of HP Mg bars in extruded, rotary-forged, and annealed conditions; EBSD and grain size analysis of HP Mg bars in (c) extruded, (d) rotary-forged, and (e) annealed conditions; (f) WAAM forming process parameter window and (g) tensile curves of AZ31 Mg alloy.

Table 5
Comparison of room-temperature tensile mechanical properties of HP Mg and commercial Mg alloys.

Product types	Tensile strength (MPa)	Yield strength (MPa)	Elongation (%)	Reduction of area (%)	Notes
HP Mg extruded bars	≥ 130	≥ 60	≥ 10	N.A.	China Nonferrous Metals Industry Standard YS/T 1313-2019
HP Mg extruded bars	≥ 130 ≥ 180	≥ 50 ≥ 100	≥ 10 ≥ 10	≥ 10 ≥ 10	Group Standard of Chinese Society for Biomaterials T/CSBM0041-2023
HP Mg extruded bars	≥ 130	≥ 60	≥ 10	N.A.	Chinese National Standard
AZ31B sheets	≥ 220	≥ 110	≥ 50	N.A.	GB/T5156-2022
M2M sheets	≥ 180	≥ 100	≥ 50	N.A.	Chinese National Standard
AZ31 sheets	≥ 225	≥ 140	≥ 50	N.A.	GB/T5154-2022
HP Mg rods (Φ18 mm)	190	80	18	22	The authors' group
HP Mg rods (Φ8 mm)	217	159	12	10	The authors' group
HP Mg rods (Φ6 mm)	190	124	11	10	The authors' group
HP Mg plates and strips (4 mm)	186	110	8.5	N.A.	The authors' group
HP Mg plates and strips (2 mm)	176	104	6	N.A.	The authors' group
HP Mg plates and strips (0.5 mm)	160	104	6	N.A.	The authors' group
HP Mg tubes (9 × 1.5 mm)	180	73	14	N.A.	The authors' group
HP Mg tubes (6 × 0.3 mm)	132–135	82–84	3–4	N.A.	The authors' group

J18 (extruded HP Mg bars) exhibits a relatively low YS (~66.2 MPa), it possesses high UTS (~180.0 MPa) and elongation (~23.8%). After rotary swaging, the YS and UTS of X10 (rotary-forged HP Mg bars) substantially increase to ~127.6 MPa and ~200.1 MPa, respectively, while elongation decreases to ~12.2%. Following further annealing, the T10 (annealed HP Mg bars) surprisingly shows that UTS can improve further to ~212.0 MPa, while YS and elongation slightly reduce to ~103.3 MPa and ~6.5%, respectively [191]. In comparison to conventional high-temperature extrusion (300–500 °C) followed by room-temperature rolling or drawing, this technique significantly improves formability, yield efficiency, and product consistency, thereby facilitating batch production. Utilizing this strengthening and toughening approach, the authors have fabricated a series of HP Mg raw materials, including sheets and strips (thickness ranging from 4 to 0.5 mm) and thin-walled tubes (*e.g.*, Φ 9 × 1.5 mm and Φ 6 × 0.25 mm). The typical mechanical properties of these sheets, strips, and tubes (Table 5) exhibit superior strength, ductility, biocompatibility, and biodegradation behavior relative to several commercial Mg alloys. The authors' group has spearheaded the development of the Chinese Society of Biomaterials standard T/CSBM0041-2023, entitled "Medical HP Mg Extruded Round Bar," thereby establishing a benchmark for quality and performance in this field.

Electrochemical testing and long-term immersion experiments are applied to assess the biodegradation performance of HP Mg across various processing states, revealing corrosion rates consistently below 0.6 mm·y^{-1}, substantially lower than those observed in cast and extruded Mg alloys. Recognizing that the biodegradation behavior of Mg-based materials markedly differs from that of conventional inert biomedical alloys (*e.g.*, titanium and cobalt-chromium alloys), the authors' group have been invited to contribute to the revision of Chapter 15, "Qualitative and Quantitative Analysis of Degradation Products of Metals and Alloys," in the 2012 edition of China's Biological Evaluation of Medical Devices (GB/T16886.15-2003). This contribution underscores the authors' expertise in addressing the unique biodegradation challenges of Mg-based materials and their implications for clinical translation.

4.1.2. Strength and toughness regulation and microscopic mechanisms of HP Mg raw materials

Mg alloys are typically fabricated as hot-worked castings or extruded components owing to their restricted room-temperature formability, significant springback (attributable to a lower elastic modulus), diminished yield rates, and an inherent susceptibility to microcracking relative to metals with cubic crystal structures such as aluminum and steel. HP Mg demonstrates markedly inferior cold workability compared to its alloyed counterparts, being characterized by coarse grains and microdefects inherent in hot-working processes. These structural imperfections not only compromise mechanical properties including tensile strength and ductility but also impede uniform and controlled *in vivo* biodegradation, which is critical for biomedical applications. To address these challenges and enhance the formability, toughness, and strength-toughness synergy of HP Mg, the authors' group has developed a strategy centered on grain refinement and coordinated activation of microscopic plastic deformation mechanisms, including slip, twinning, and stacking faults (SFs), as illustrated in Fig. 9c and e. Fig. 9c shows that J18 consists of equiaxed α-Mg grains, indicating complete recrystallization during warm extrusion. In X10 (Fig. 9d), fine grains appear along coarse grain boundaries, with the uniform color suggesting low-angle grain boundaries formed *via* dislocation accumulation. After annealing, T10 (Fig. 9e) exhibits coarser equiaxed grains due to recrystallization and grain growth. Pole figures (Fig. 9c and e) show weak textures in all samples due to high-temperature processing and symmetric deformation. Grain size analysis reveals an upward trend of X10, J18, and T10, confirming that rotary swaging refines grains, while annealing induces coarsening [191].

At the macroscopic scale, as-cast HP Mg ingots typically exhibit a coarse-grained microstructure (500 μm–5 mm). By applying triaxial compressive stress, unlike conventional rolling and drawing, which impose biaxial compression and uniaxial tension, uniform plastic deformation is achieved. This process effectively fragments and refines the coarse grain structure, while minimizing the formation of microdefects, resulting in a minimum grain size below 10 μm and an average grain size of grade 8 to 10. At the microscopic level, despite the inherently high SF energy of pure Mg, the authors' approach induces the formation of high-density, broad SFs via sequential grain refinement and tempering. These SFs augment both the strengthening effect and the plastic deformation capacity, thereby mitigating the loss of ductility typically associated with grain coarsening. During deformation, these SFs act as barriers to dislocation motion, enhancing mechanical strength, while maintaining toughness. This integrated methodology overcomes the conventional strength-toughness trade-off, achieving yield rates surpassing 80% and markedly enhancing product quality.

4.2. Performance evaluation of typical orthopedic repair products from additive manufactured HP Mg and matching welding wires

WAAM presents significant advantages over laser and electron beam forming techniques, notably reduced operational costs and improved forming efficiency. For highly reactive Mg products, wire-based additive manufacturing offers enhanced safety and practicality compared to powder-based methods, thereby mitigating risks associated with tendency of Mg for combustion and explosion. Nonetheless, achieving a uniform microstructure and consistent mechanical properties in WAAM-fabricated Mg components remains challenging primarily due to the metal's elevated thermal conductivity and substantial heat capacity. To address these limitations, the authors' group have collaborated with the Welding Institute of Guangdong Academy of Sciences to develop an economical WAAM system specifically designed for Mg and other metal wire-based additive manufacturing processes. This system supports both the development and batch production of Mg-based components, integrating advanced features to optimize forming conditions. A temperature sensor, strategically positioned at the apex of the workspace, dynamically regulates the forming temperature of Mg, minimizing thermally induced defects and ensuring quality consistency. Additionally, a dedicated inert gas channel combined with a transparent protective shield facilitates real-time visual monitoring of processing under a controlled inert atmosphere, effectively reducing porosity in Mg prints produced in air. To complement the WAAM process, a patented "rotary swaging and drawing" technique has been developed, enabling the production of high-quality, cost-effective, HP Mg and its alloy fine wires with a diameter of less than 2 mm at temperatures ranging from ambient to 200 °C. In contrast to the spherical Mg powders required for powder-based laser printing, this proprietary wire offers substantial cost savings, while fully meeting the requirements of 3D wire printing, repair of large Mg alloy castings, and diverse industrial applications. Utilizing HP Mg wires, printing experiments were conducted to evaluate the microstructure and mechanical properties of the resulting components. A scientifically optimized processing window was established, achieving an effective deposition rate of up to 89% and a relative density of 98%. Chemical composition analysis reveals negligible deviations between the original wire and printed Mg. The printed sample exhibits a tensile strength of 245 MPa, comparable to that of human cortical bone and more than double that of as-cast AZ31 alloy (~115 MPa). This mechanical performance aligns closely with that of AZ31B wrought Mg alloy plates specified in the GB/T 5154-2010 standard (Fig. 9g). This work represents a pioneering breakthrough in the fabrication of high-quality surgical implants using low-cost wire-based arc printing. For example, the WAAM-fabricated AZ31 alloy components demonstrated tensile strength superior to that of the commercial AZ31 forgings and extrusions, along with reduced gaseous impurity content (Table 6).

Table 6
Mechanical properties of AZ31 alloy WAAM printed parts.

Mechanical properties	WAAM-AZ31	As-cast AZ31	As-extruded AZ31
Yield strength (MPa)	113	80	150
Tensile strength (MPa)	235	170	230
Elongation (%)	27	4–10	18–25
Hardness (HV)	53	48	53

Microstructural analysis of the printed material revealed a uniform morphology characterized by isotropic crystal grains, with an average grain size ranging from 6.9 to 12 μm, accompanied by trace precipitates of the $Mg_{17}Al_{12}$ and $Al_{86}Mn_{14}$ phases. Although the corrosion performance of the WAAM-processed AZ31 was slightly inferior to that of traditionally cast counterparts, it exhibited enhanced stability. This behavior is attributed to a transition in the corrosion mechanism from micro-galvanic corrosion, common in cast materials, to intergranular corrosion driven by the refined grain structure [98]. These findings underscore the potential of the developed WAAM system and wire production technique to advance the clinical translation of Mg-based biodegradable implants, offering an optimal balance of cost-efficiency, mechanical robustness, and microstructural uniformity for biomedical applications.

4.3. Surface coatings on Mg alloys

4.3.1. Inorganic coatings

Inorganic coatings significantly enhance the corrosion resistance and mechanical integrity of Mg-based biodegradable metals, making them highly suitable for the complex physiological environments encountered in biomedical applications. To this end, the authors' group has developed an innovative $Mg_3(PO_4)_2$ pretreatment layer to augment the corrosion resistance of a $Ca_3(PO_4)_2$ coating on WE43 alloy. This approach results in a uniform and dense $Ca_3(PO_4)_2$ coating, reducing

the corrosion rate by 77% [192]. Additionally, an HA coating has been fabricated *via* chemical solution deposition, with optimized concentrations of EDTA-Ca and KH_2PO_4 promoting the formation of a robust bilayer structure comprising a thicker $Mg(OH)_2$ inner layer and a thinner HA outer layer, thereby improving both corrosion resistance and biocompatibility [193]. A composite coating of titania-Zn phosphate and nanocrystalline Zn has also been developed, reducing the corrosion current density of WE43 alloy from 151.1 to 4.1 $\mu A \cdot cm^{-2}$, significantly enhancing its corrosion resistance [194]. Furthermore, a Ca-Zn-P composite coating, synthesized via hydrothermal treatment on Zn-pretreated WE43 alloy, lowers the corrosion current density to 3.49×10^{-5} $A \cdot cm^{-2}$, while increasing the charge transfer resistance to 1.22×10^5 $\Omega \cdot cm^2$ [195]. Using radio-frequency magnetron sputtering, a composite film of SnO_2 and SnO was deposited on Mg-Y-RE alloy, achieving a 345-fold reduction in corrosion current density and a 1000-fold increase in charge transfer resistance. This coating also enhanced the adhesion and proliferation of MC3T3-E1 pre-osteoblasts, as evidenced by cellular assays (Fig. 10a) [196]. Similarly, a Zr-based nanostructured coating, fabricated by magnetron sputtering on Mg_4Y-3RE alloy, significantly reduced the corrosion current density, increased charge transfer resistance, inhibited corrosion propagation, and slowed the dissolution rate of the Mg alloy in simulated body fluids [197]. An *in situ* Sr-Zn based phosphate coating applied to the Zn-electroplated WE43 alloy further reduced the corrosion current density to 0.21 $\mu A \cdot cm^{-2}$ and raised the charge transfer resistance to 1.22×10^5 $\Omega \cdot cm^2$, while achieving cell viability exceeding 100% [198]. These advancements collectively demonstrate effective strategies to mitigate corrosion of Mg-based biodegradable metals, establishing a robust foundation for integrating complementary coating technologies to optimize their mechanical properties, biodegradation kinetics, and biocompatibility for clinical translation.

4.3.2. Organic coatings

Organic coatings facilitate precise control over biodegradation kinetics by employing tunable polymers, thereby extending the functional lifespan of Mg-based biodegradable metals. These coatings exhibit excellent biocompatibility, promoting cell adhesion and proliferation, and can be engineered for drug delivery to impart multifunctionality that addresses diverse clinical requirements. To enhance the performance of these polymer-based systems, a PDA/alginate (ALG) composite coating has been developed on HP Mg. The fabrication process entails the initial deposition of a PDA intermediate layer, followed by spin-coating with ALG, resulting in a uniform composite coating with a thickness of approximately 8.6 μm. Electrochemical analysis demonstrated that the PDA interlayer markedly improved the adhesion of the ALG coating to the Mg substrate, reducing the corrosion current density by over one order of magnitude and increasing the charge transfer resistance by 12-fold, thereby substantially enhancing corrosion resistance. Immersion tests further confirmed that the PDA/ALG coating effectively modulated the biodegradation rate of the Mg alloy, established a mildly alkaline microenvironment favorable for cell proliferation and bone tissue regeneration, while concurrently improving wear resistance [199]. These findings establish the deposition of a PDA intermediate layer as an effective strategy for tailoring the corrosion behavior of ALG-coated Mg substrates, underscoring its significant potential for orthopedic implant applications. Consequently, the PDA/ALG composite coating not only markedly enhances the corrosion resistance and mechanical integrity of Mg-based materials but also fosters favorable conditions for cellular growth and tissue repair, thereby providing a robust foundation for the clinical translation of Mg-based biodegradable metals.

4.3.3. Composite coatings

Composite coatings synergistically integrate the advantages of both organic and inorganic systems, delivering robust corrosion protection and enhanced bio-integration, while optimizing the performance of Mg alloys in the complex physiological environment. Through a series of advanced coating strategies, the corrosion resistance and biocompatibility of Mg-based biodegradable metals have been substantially improved. Initially, β-TCP/ALG composite microspheres were investigated for multi-drug release and bone regeneration applications (Fig. 10b). A negative correlation between microsphere size and drug-loading capacity was observed, with the system demonstrating excellent cytocompatibility and significantly promoting bone regeneration. However, further refinement of drug release kinetics remains necessary [200]. Additionally, a silane-containing transition layer/sodium alginate composite coating, applied *via* spin-coating onto alkalized HP Mg, reduced the corrosion current density from 130.9 to 1.3 $\mu A \cdot cm^{-2}$, increased the charge transfer resistance by 190-fold, and decreased the biodegradation rate from 3.47 to 0.80 $mm \cdot y^{-1}$ [201]. Additionally, the PLA coating with a (3-aminopropyl)triethoxysilane (ATS) transition layer on AZ31B alloy pre-treated with Mg-Al layered double hydroxide (LDH) further reduced the corrosion current density to 0.6 $\mu A \cdot cm^{-2}$ and elevated the charge transfer resistance to 1.05×10^5 $\Omega \cdot cm^2$, effectively suppressing corrosion propagation and hydrogen evolution (Fig. 10b) [202]. Moreover, a poly(1,3-trimethylene carbonate) (PTMC) composite coating, developed by MAO for vascular stents, sealed the porous MAO layer, significantly reducing Mg^{2+} release and local pH elevation, thereby enhancing corrosion resistance and cytocompatibility [203]. Further advancements involve the integration of nanostructured materials into polymer matrices. PDA-modified zeolitic imidazolate framework-8 (PZIF-8) nanoparticles were incorporated into a polycaprolactone (PCL) coating to enhance the coating density and biomineralization capacity. This modification significantly improved the corrosion resistance, upregulated osteogenesis-related gene expression, and demonstrated superior bone reconstruction in a rabbit bone defect model (Fig. 10c and d) [204]. Additionally, a composite coating comprising hydroxide nanosheets, ATS, and PLLA reduced the corrosion current density from 1.3×10^{-4} to 1.8×10^{-9} $A \cdot cm^{-2}$, while exhibiting excellent cytocompatibility with MC3T3-E1 osteoblasts [205]. Through

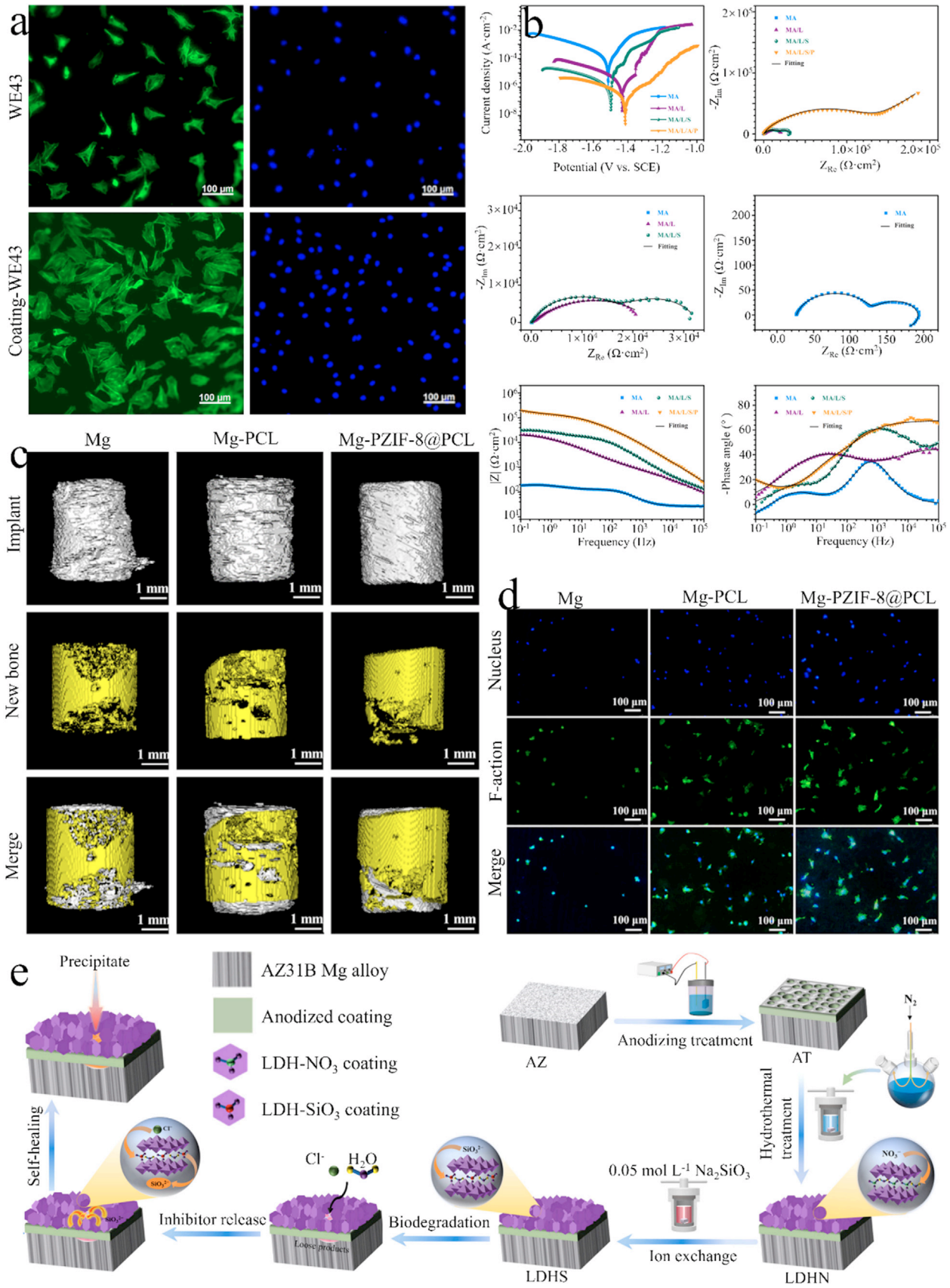

Fig. 10. (a) Fluorescence images of MC3T3-E1 pre-osteoblast cells after 6-hour incubation on bare and coated-WE43 Mg alloy; (b) electrochemical test results of MA (AZ31B Mg alloy), MA/L, MA/L/S and MA/L/S/P; (c) micro-CT images of *in vivo* implants and (d) *in vitro* cellular fluorescence morphology for Mg, Mg-PCL, and Mg-PZIF-8@PCL; (e) schematic diagram showing the fabrication and self-healing mechanism of the smart LDH-SiO_3 coating on AZ31B Mg alloy.

the systematic development and optimization of these composite coating technologies, the corrosion resistance, mechanical integrity, and biocompatibility of Mg-based biodegradable metals have been significantly enhanced. These innovations establish a solid foundation for the clinical translation of Mg-based materials, showcasing their broad potential in biomedical implant applications.

4.3.4. Self-healing coatings

Self-healing coatings possess the ability to autonomously repair damage, substantially extending the functional lifespan of Mg-based biodegradable metals. By restoring coating integrity through intelligently designed structures in response to mechanical or chemical insult, these coatings enhance material stability and reliability in the dynamic physiological environment, thereby reducing maintenance needs and making them ideal for long-term implant applications. To this end, a Mg-Al layered double hydroxide coating intercalated with silicate ions (LDH-SiO_3) has been developed on the anodized AZ31B alloy. Utilizing hydrothermal treatment and anion exchange, a bilayer architecture was formed, comprising a dense inner layer and a porous outer layer. The dense inner layer effectively impedes the ingress of corrosive media, while the porous outer layer facilitates ion exchange and imparts self-healing functionality. Experimental analysis demonstrated that the LDH-SiO_3 coating significantly reduced the biodegradation rate of AZ31B alloy and enabled self-healing of localized corrosion sites through the release of SiO_3^{2-}, which reacted with dissolved Mg^{2+} to form $MgSiO_3$ precipitates (Fig. 10e). Furthermore, the coating promoted adhesion and proliferation of MC3T3-E1 pre-osteoblast cells, exhibiting excellent biocompatibility [206]. This intelligent coating strategy addresses critical limitations of conventional coatings, such as the absence of self-healing capacity and potential biotoxicity, while offering a novel approach to the development of Mg-based biomedical implants. Consequently, the LDH-SiO_3 functional coating, with its distinctive bilayer design, significantly enhances the corrosion resistance and biocompatibility of Mg-based materials, demonstrating exceptional self-healing capacity and great potential for bone tissue regeneration. This advancement provides robust assurance for the safety and efficacy of Mg-based biodegradable metals in clinical translation.

4.4. Development of typical Mg alloy orthopedic and dental biomedical devices

4.4.1. Bone plates

Bone plates represent one of the most widely used surgical implants for the treatment of bone defects, providing robust mechanical support to stabilize fracture ends or defect sites, thereby preventing displacement and promoting optimal bone healing. A stable fixation environment further enhances osteoblast proliferation and new bone formation, accelerating the regeneration and repair of bone tissue. Currently, titanium alloys dominate clinical applications for bone plates due to their outstanding mechanical properties and excellent biocompatibility. However, their application is limited by challenges such as stress shielding and need for secondary surgical intervention for removal. To address these issues, a novel degradable Mg-3Zn alloy bone plate has been designed and fabricated, including both raw and finished forms, using an in-house developed WAAM process. Systematic evaluations of its mechanical properties, biodegradation behavior, and antibacterial performance were conducted compared to AZ31 alloy. Mechanical testing revealed that the tensile strength and elastic modulus of Mg-3Zn alloy closely matched the mechanical properties of human cortical bone. Biodegradation assessments indicated that the corrosion current density of the WAAM-fabricated Mg-3Zn was comparable to that of as-cast AZ31. Additionally, antibacterial assays demonstrated the superior performance of the WAAM-fabricated Mg-3Zn, achieving an antibacterial rate of 99.41 $\pm$ 0.13%, which substantially outperformed as-cast AZ31 with an antibacterial rate of 91.15 $\pm$ 1.10%. These findings highlight the potential of the Mg-3Zn alloy bone plate as a biodegradable alternative, offering a balance of mechanical integrity, controlled biodegradation, and enhanced antibacterial efficacy, making it highly suitable for clinical applications.

4.4.2. Porous bone scaffolds

Porous ceramic scaffolds for bone repair are inherently limited by poor toughness, brittleness, and significant challenges in fabricating large-scale, personalized constructs tailored to specific bone defects. Biodegradable metal-based bioceramic porous scaffolds address these limitations by enhancing the strength and toughness of ceramic frameworks, while generating a mildly alkaline microenvironment through the biodegradation of elements such as Mg and Zn, which promotes osteogenic activity at bone defect sites. Furthermore, their interconnected three-dimensional porous architecture facilitates both osteo-induction and osteo-conduction, positioning them as a critical focus for the future development of solutions aiming at repairing large bone defects. Conventional fabrication techniques such as powder metallurgy and powder-based additive manufacturing heavily rely on biodegradable metal powders. However, the production of these powders is limited by high reactivity, technical complexity, and protracted preparation cycles, which hinder rapid performance evaluation, product development, and industrial-scale implementation of these innovative scaffolds. To overcome these challenges, composite wires consisting of biodegradable metals such as Mg alloys incorporated with bio-ceramics and pore-forming agents have been employed as raw materials. Utilizing wire-based 3D printing equipment, personalized preforms of various geometries are initially fabricated, followed by sintering and pore-forming processes, with ultrasonic cleaning applied as a post-treatment to introduce internal porosity. This approach enables the rapid, efficient, and cost-effective production of biodegradable metal-based bioceramic porous bone scaffolds (the Chinese Invention Patent number is ZL202110089285.0), meeting the stringent requirements of biomedical engineering for the development and application of advanced porous constructs for bone repair.

4.4.3. GBR membranes

GBR membranes have gained prominence in periodontal and bone regeneration therapies due to their proven efficacy, prompting the development of a new generation of biodegradable Mg alloy GBR membranes in Europe. These advanced membranes offer significant advantages over traditional non-biodegradable GBR products. Current research efforts focus on the innovative design and advanced processing of Mg-based GBR membranes, with an emphasis on material selection, structural optimization, surface modification, and porosity engineering. These strategies aim to overcome the limitations of existing Mg-based GBR membranes, particularly in terms of biodegradation kinetics, biocompatibility, and mechanical performance. A biodegradable pure Mg dental screw, designed for integration with GBR applications, has been submitted for a Chinese Invention Patent (CN202310721814.3). The design and development concepts for this novel Mg-based GBR membrane are detailed as follows.

(1) Material selection and design
The self-developed high-strength-to-weight ratio, HP Mg sheet and strip materials are selected as the primary material. Research focuses on optimizing the balance between strength and toughness, alongside formability, with comparative analyses conducted against clinically approved pure Mg materials utilized internationally.
(2) Product structural design
Two structural configurations, dense and porous, will be engineered for comparative evaluation. The porous structure will be fabricated using advanced techniques such as laser etching and chemical milling to create a hierarchical pore size distribution at nanoscale and microscale levels. This design enhances cell infiltration and tissue mineralization, which are critical for effective bone regeneration.
(3) Surface modification and functionalization
Single- and double-sided surface treatments will be applied to functionalize the GBR membranes. Beyond developing bioactive surface layers to enhance biocompatibility and mineralization capacity, antibacterial elements will be incorporated to improve the membrane's antibacterial efficacy, addressing clinical infection risks.
(4) *In vitro* and *in vivo* validation
In vitro assessments and animal experiments will be conducted to refine the mechanical properties, formability, and biodegradation behavior of the membranes. These evaluations will ensure that the GBR membranes maintain structural integrity and biological safety throughout the bone regeneration process, aligning with clinical requirements.

These advancements collectively position the Mg-based GBR membrane as a promising candidate for next-generation periodontal and bone regeneration therapies, offering improved biodegradation control, biocompatibility, and mechanical stability over existing solutions.

5. Summary and outlook

Mg and its alloys are emerging as compelling candidates for next-generation biodegradable implantable medical devices, particularly in orthopedic, dental, and cardiovascular applications. This prominence stems from their advantageous intrinsic properties, including low density, an elastic modulus closely approximating that of bone tissue, inherent biodegradability *in vivo*, and beneficial biological functionalities such as osteo-induction and antimicrobial effects. This review synthesizes recent advancements in the field, critically evaluating novel Mg-based materials, processing technologies, and device development strategies. Key areas including alloying, fabrication techniques, purification, surface modification, and structural design are comprehensively discussed to provide insights into the current research landscape and guide future investigations into biodegradable metallic biomaterials. Salient considerations and forward-looking recommendations are subsequently outlined.

(1) Alloying
Alloying strategies are pivotal for enhancing the mechanical performance of Mg, primarily by modulating microstructural evolution within the matrix and activating pertinent strengthening mechanisms (*e.g.*, solid solution strengthening, precipitation hardening). Concurrently, manipulating corrosion mechanisms can alter the properties of biodegradation products and moderate the overall biodegradation rate. A critical translational challenge, however, arises from the concurrent dissolution of alloying elements with the Mg matrix *in vivo*. Excessive localized concentrations of certain elements may pose risks to human health. Consequently, careful consideration of alloying element selection, precise control over their concentrations, and rigorous assessment of their biocompatibility are paramount for clinical success.
(2) Fabrication techniques
Fabrication techniques like casting and powder metallurgy along with emerging methods like AM, are pivotal for fabricating Mg-based alloys and devices. Each methodology possesses distinct advantages and inherent limitations. Notably, AM technologies offer exceptional versatility for creating patient-specific implants with intricate architectures tailored to complex anatomical defects, thereby addressing specific patient needs.
(3) Purification
Advanced purification processes, including filtration, electromagnetic purification, and melt self-purification, enable the production of HP Mg-based biodegradable metals. These techniques significantly reduce biodegradation rates and improve the biocompatibility of corrosion products, thereby enhancing the safety and longevity of surgical implants.
(4) Surface modification
Surface modification strategies effectively regulate biodegradation kinetics and improve the biocompatibil-

ity of Mg-based metals. By enhancing corrosion resistance and stability in physiological conditions, these strategies promote cell proliferation and tissue regeneration, thereby broadening the clinical applicability of Mg-based implants.

(5) Structural design
Porous structures increase surface area and facilitate nutrient transport, thereby enhancing biocompatibility and osseointegration. Additionally, fine-grained structures improve strength and ductility, thereby delaying biodegradation, whereas composite structures with bioceramic reinforcements permit the tailoring of mechanical and corrosion properties, supporting the development of a wide range of orthopedic and dental devices.

Despite these advancements, further exploration remains warranted. Five key opportunities and challenges are identified for the future development of biomedical Mg and its alloys as follows.

(1) Harnessing the potential of biomedical Mg alloy materials
China possesses abundant Mg resources and leads global production of primary Mg, yet its exports remain dominated by low-value commodity ingots. Although China's fundamental research in novel medical Mg alloys is progressing concurrently with international efforts, the development pipeline and clinical adoption of high-specification raw materials and derivative medical devices exhibit a relative lag. Leveraging China's strategic national focus on advanced biomaterials, high-end medical devices, and advanced manufacturing presents a critical opportunity and strategic imperative to convert resource advantage into technological and economic leadership through accelerated R&D and application translation in the medical Mg sector, which holds considerable promise. A pivotal hurdle in this pursuit is developing scalable, high-purity alloy production and precision manufacturing techniques that meet biomedical devices' stringent quality standards, essential for producing high-value implants rather than raw materials.

(2) Prioritizing performance-cost synergy in material design
Future design criteria for next-generation biodegradable metals must prioritize enhancing properties such as cold workability while achieving an optimal balance between strength and toughness for Mg and its alloys. Simultaneously, a holistic design philosophy is required, integrating considerations of the product's form, intrinsic properties, functional performance, clinical efficacy, and overall value/cost-effectiveness. This necessitates a forward-looking yet pragmatic approach that addresses critical lifecycle factors including operational reliability, manufacturing accessibility, low cost, processability, user-friendliness, traceability, and regulatory compliance. Consequently, a key research gap lies in designing alloys that are biocompatible yet inherently amenable to cost-effective, high-throughput secondary processing such as extrusion and wire drawing, which are critical for manufacturing medical devices like orthopedic screws, GBR membranes, and cardiovascular stents.

(3) Controlling biodegradation and ensuring host compatibility
The *in vivo* biodegradation profile is inextricably linked not only to the material's intrinsic composition and microstructure but also critically depends on extrinsic host factors, the specific implantation microenvironment, and the intended clinical application. Consequently, research must transcend material characterization per se to encompass a deeper understanding of tissue healing dynamics across different anatomical sites and establish relevant tissue resorption tolerance rates. This knowledge is essential for accurately benchmarking biodegradation data, tailoring material corrosion profiles to diverse clinical scenarios, optimizing cellular responses, and minimizing potential adverse effects such as cytotoxicity and excessive inflammation. To address material-host complexity, a critical future direction involves developing multivariate models that correlate initial alloy microstructure and surface properties with local *in vivo* degradation dynamics (*e.g.*, H_2 evolution, Mg^{2+} release, pH fluctuations, etc.) and subsequent cellular responses, advancing beyond simplistic mass loss metrics.

(4) Establishing standardized international protocols
The development and global adoption of consensus-based, standardized protocols are indispensable for rigorously evaluating the *in vitro* and *in vivo* biodegradation behavior of novel biodegradable metallic materials and implant systems. Such standards are crucial prerequisites for providing reliable guidance for material evaluation and subsequent clinical translation efforts. The current lack of standardized assessment methodologies poses a significant impediment to navigating diverse international regulatory landscapes and achieving successful market entry. Furthermore, internationally harmonized standards will serve a vital role in guiding research priorities, enabling robust cross-study comparisons, facilitating the identification of critical knowledge gaps and technical hurdles, and ultimately accelerating the innovation cycle, clinical translation, and broader dissemination of biodegradable metal technologies. A critical step toward establishing robust standards involves creating advanced *in vitro* test solutions that physiologically replicate specific implantation sites such as a simulated bone fracture environment with dynamic flow and relevant cell types, which would significantly improve currently poor *in vitro* and *in vivo* correlation.

(5) Fostering interdisciplinary collaboration across the value chain
Biodegradable metals constitute a unique class of biomaterials engineered for integrated structural and biological functionality. However, numerous scientific questions remain unanswered, and significant hurdles

impede their seamless clinical translation and commercialization. Successfully bridging the gap from fundamental discovery to widespread clinical impact necessitates synergistic, multidisciplinary collaboration among diverse stakeholders spanning the entire translational continuum (industry, academia, research institutions, clinical medicine, and regulatory/testing bodies). This integrated approach, encompassing R&D, manufacturing, quality control, clinical evaluation, and post-market surveillance, is essential to expedite the development of these advanced materials, positioning them to eventually augment or supplant conventional metallic implants (*e.g.*, titanium, cobalt-chromium alloys), thereby delivering substantial benefits to patients and contributing positively to public health outcomes. To make such collaboration effective, a concrete objective should be the co-development of "bio-instructive" surfaces on existing Mg alloy material platforms. This specific challenge requires that materials scientists create stable functionalization, biologists identify optimal signaling molecules, among other critical tasks, while engineers ensure the final product is manufacturable and cost-effective.

Declaration of competing interest

The authors declare that they have no known competing financial interests or personal relationships that could have appeared to influence the work reported in this paper.

CRediT authorship contribution statement

Jianzeng Ren: Writing – original draft, Methodology, Formal analysis, Data curation, Conceptualization. **Zhou Jiang:** Investigation, Formal analysis, Data curation. **Jianbing He:** Software, Methodology, Formal analysis. **Xiaoying Wang:** Visualization, Supervision, Methodology. **Weihong Jin:** Writing – review & editing, Supervision, Funding acquisition, Formal analysis, Data curation. **Zhentao Yu:** Writing – review & editing, Validation, Methodology, Funding acquisition.

Acknowledgments

This work was financially supported by the Science and Technology Planning Project of Guangdong Province (Nos. 2024A0505040016 and 2023A0505050148), National Key Research and Development Project of China (2023YFB3809900/2023YFB3809902), and Natural Science Foundation of Guangdong Province (No. 2025A1515010026).

References

[1] J.L. Wang, J.K. Xu, C. Hopkins, D.H.K. Chow, L. Qin, Adv. Sci. 7 (8) (2020) 1902443.
[2] S. Seetharaman, D. Sankaranarayanan, M. Gupta, J. Func. Biomater. 14 (6) (2023) 324.
[3] C. Li, C. Guo, V. Fitzpatrick, A. Ibrahim, M.J. Zwierstra, P. Hanna, A. Lechtig, A. Nazarian, S.J. Lin, D.L. Kaplan, Nat. Rev. Mater. 5 (1) (2020) 61–81.
[4] Y.F. Zheng, X. Liu, D.N. Shen, W.T. Li, Y. Cheng, M. Yang, Y.H. Kou, B.G. Jiang, J. Mater. Sci. Technol. 147 (2023) 132–144.
[5] L.F. Velásquez-Garcí, Y. Kornbluth, Annu. Rev. Biomed. Eng. 23 (1) (2021) 307–338.
[6] W. Liang, C. Zhou, H. Zhang, J. Bai, B. Jiang, C. Jiang, W. Ming, H. Zhang, H. Long, X. Huang, J. Biol. Eng. 17 (1) (2023) 56.
[7] J.C. Paiva, L. Oliveira, M.F. Vaz, S. Costa-de-Oliveira, Bioengineering 9 (8) (2022) 409.
[8] M. Yazdimamaghani, M. Razavi, D. Vashaee, K. Moharamzadeh, A.R. Boccaccini, L. Tayebi, Mater. Sci. Eng. C 71 (1) (2017) 1253–1266.
[9] X.J. Xing, Y. Han, H. Cheng, Int. J. Biol. Macromol. 240 (2023) 124407.
[10] M.S.B. Reddy, D. Ponnamma, R. Choudhary, K.K. Sadasivuni, Polymers (Basel) 13 (7) (2021) 1105.
[11] L. Wang, X.L. Guo, J.Q. Chen, Z. Zhen, B. Cao, W.Q. Wan, Y.D. Dou, H.B. Pan, F. Xu, Z.P. Zhang, J.M. Wang, D.S. Li, Q.Y. Guo, Q. Jiang, Y.N. Du, J.K. Yu, B.C. Heng, Q.Q. Han, Z.G. Ge, Bioact. Mater. 9 (2022) 332–342.
[12] M.S. Hasan, I. Ahmed, A.J. Parsons, C.D. Rudd, G.S. Walker, C.A. Scotchford, J. Biomater. Appl. 28 (3) (2013) 354–366.
[13] M. Sikora-Jasinska, P. Chevallier, S. Turgeon, C. Paternoster, E. Mostaed, M. Vedani, D. Mantovani, RSC Adv 8 (18) (2018) 9627–9639.
[14] A. Myrissa, N.A. Agha, Y. Lu, E. Martinelli, J. Eichler, G. Szakacs, C. Kleinhans, R. Willumeit-Römer, U. Schäfer, A.M. Weinberg, Mater. Sci. Eng. C 61 (1) (2016) 865–874.
[15] A.J. Drelich, S. Zhao, R.J. Guillory II, J.W. Drelich, J. Goldman, Acta Biomater 58 (2017) 539–549.
[16] H. Wang, Y. Zheng, J. Liu, C. Jiang, Y. Li, Mater. Sci. Eng. C 71 (1) (2017) 60–66.
[17] Y. Liu, Y. Zheng, X.H. Chen, J.A. Yang, H. Pan, D. Chen, L. Wang, J. Zhang, D. Zhu, S. Wu, Adv. Funct. Mater. 29 (18) (2019) 1805402.
[18] M. Razavi, M. Fathi, O. Savabi, S.M. Razavi, F. Heidari, M. Manshaei, D. Vashaee, L. Tayebi, Appl. Surf. Sci. 313 (15) (2014) 60–66.
[19] W. Lin, G. Zhang, P. Cao, D. Zhang, Y. Zheng, R. Wu, L. Qin, G. Wang, T. Wen, J. Biomed. Mater. Res. B Appl. Biomater. 103 (4) (2015) 764–776.
[20] H. Gong, K. Wang, R. Strich, J.G. Zhou, J. Biomed. Mater. Res. B Appl. Biomater. 103 (8) (2015) 1632–1640.
[21] R. Hänsch, R.R. Mendel, Curr. Opin. Plant Biol. 12 (3) (2009) 259–266.
[22] X. Gu, W. Zheng, Y. Cheng, Y. Zheng, Acta Biomater 5 (7) (2009) 2790–2799.
[23] Z. Seyedraoufi, S. Mirdamadi, J. Mech. Behav. Biomed. Mater. 21 (2013) 1–8.
[24] X. Gu, X. Xie, N. Li, Y. Zheng, L. Qin, Acta Biomater 8 (6) (2012) 2360–2374.
[25] H. Li, X. Xie, Y. Zheng, Y. Cong, F. Zhou, K. Qiu, X. Wang, S. Chen, L. Huang, L. Tian, Sci Rep. 5 (2015) 10719.
[26] R. Yue, H. Huang, G. Ke, H. Zhang, J. Pei, G. Xue, G. Yuan, Mater. Charact. 134 (2017) 114–122.
[27] J. Kubásek, D. Vojtěch, E. Jablonská, I. Pospíšilová, J. Lipov, T. Ruml, Mater. Sci. Eng. C 58 (1) (2016) 24–35.
[28] M. Schinhammer, A.C. Hänzi, J.F. Löffler, P.J. Uggowitzer, Acta Biomater 6 (5) (2010) 1705–1713.
[29] H. Hermawan, A. Purnama, D. Dube, J. Couet, D. Mantovani, Acta Biomater 6 (5) (2010) 1852–1860.
[30] B. Liu, Y. Zheng, Acta Biomater 7 (3) (2011) 1407–1420.
[31] N. Zhao, D. Zhu, Int. J. Biomed. Eng. Technol. 12 (4) (2013) 382–398.
[32] E.C. Huse, Chicago Med. J. Exam. 37 (2) (1878) 171–172.
[33] B. Heublein, R. Rohde, V. Kaese, M. Niemeyer, W. Hartung, A. Haverich, Heart 89 (6) (2003) 651–656.
[34] M.S. Song, R.C. Zeng, Y.F. Ding, R.W. Li, M. Easton, I. Cole, N. Birbilis, X.B. Chen, J. Mater. Sci. Technol. 35 (4) (2019) 535–544.
[35] T. Kraus, S.F. Fischerauer, A.C. Hänzi, P.J. Uggowitzer, J.F. Löffler, A.M. Weinberg, Acta Biomater 8 (3) (2012) 1230–1238.

[36] M.M. Zerankeshi, R. Alizadeh, E. Gerashi, M. Asadollahi, T.G. Langdon, J. Magnes. Alloy. 10 (7) (2022) 1737–1785.
[37] C. Shuai, S. Li, S. Peng, P. Feng, Y. Lai, C. Gao, Mater. Chem. Front. 3 (4) (2019) 544–562.
[38] G. Li, H. Yang, Y. Zheng, X.-H. Chen, J.-A. Yang, D. Zhu, L. Ruan, K. Takashima, Acta Biomater 97 (1) (2019) 23–45.
[39] P.K. Bowen, E.R. Shearier, S. Zhao, R.J. Guillory, F. Zhao, J. Goldman, J.W. Drelich, Adv. Healthcare Mater. 5 (10) (2016) 1121–1140.
[40] P.K. Bowen, J. Drelich, J. Goldman, Adv. Mater. 25 (18) (2013) 2577–2582.
[41] H.J. Seo, Y.E. Cho, T. Kim, H.I. Shin, I.S. Kwun, Nutr. Res. Pract. 4 (5) (2010) 356.
[42] B. Jia, H. Yang, Y. Han, Z. Zhang, X. Qu, Y. Zhuang, Q. Wu, Y. Zheng, K. Dai, Acta Biomater 108 (2020) 358–372.
[43] J.M. Seitz, M. Durisin, J. Goldman, J.W. Drelich, Adv. Healthcare Mater. 4 (13) (2015) 1915–1936.
[44] M. Asgari, R. Hang, C. Wang, Z. Yu, Z. Li, Y. Xiao, Metals (Basel) 8 (4) (2018) 212.
[45] M. Peuster, P. Wohlsein, M. Brügmann, M. Ehlerding, K. Seidler, C. Fink, H. Brauer, A. Fischer, G. Hausdorf, Heart 86 (5) (2001) 563–569.
[46] W. Zhang, X. Gao, H. Zhang, G. Sun, G. Zhang, X. Li, H. Qi, J. Guo, L. Qin, D. Shi, Nat. Commun. 15 (1) (2024) 7903.
[47] T. Kraus, F. Moszner, S. Fischerauer, M. Fiedler, E. Martinelli, J. Eichler, F. Witte, E. Willbold, M. Schinhammer, M. Meischel, Acta Biomater 10 (7) (2014) 3346–3353.
[48] J. Gonzalez, R.Q. Hou, E.P. Nidadavolu, R. Willumeit-Römer, F. Feyerabend, Bioact. Mater. 3 (2) (2018) 174–185.
[49] D. Li, D. Zhang, Q. Yuan, L. Liu, H. Li, L. Xiong, X. Guo, Y. Yan, K. Yu, Y. Dai, Acta Biomater 141 (15) (2022) 454–465.
[50] P.K. Bowen, J. Drelich, J. Goldman, Mater. Sci. Eng. C 33 (8) (2013) 5064–5070.
[51] Y. Wu, Y. Wang, D. Zhao, N. Zhang, H. Li, J. Li, Y. Wang, Y. Zhao, J. Yan, Y. Zhou, Colloids Surf., B 181 (1) (2019) 349–359.
[52] H.J. Yu, J.Q. Wang, X.T. Shi, D.V. Louzguine-Luzgin, H.K. Wu, J.H. Perepezko, Adv. Funct. Mater. 23 (38) (2013) 4793–4800.
[53] L.V. Maximiano, L.B. Correa, N.C. Gomes-da-Silva, L.S. da Costa, M.G.P. Da Silva, A.V. Chaves, M.L. Franco, P.B.A. Fechine, A.S. de Menezes, R. Santos-Oliveira, Colloids Surf., B 239 (2024) 113931.
[54] A. Zarei, A. Farazin, J. Aust. Ceram. Soc. 61 (2025) 797–813.
[55] Z. Xi, Y. Wu, S. Xiang, C. Sun, Y. Wang, H. Yu, Y. Fu, X. Wang, J. Yan, D. Zhao, ACS Omega 5 (9) (2020) 4548–4557.
[56] H. Kabir, K. Munir, C. Wen, Y. Li, Bioact. Mater. 6 (3) (2021) 836–879.
[57] J. Venezuela, M. Dargusch, Acta Biomater 87 (15) (2019) 1–40.
[58] D. Persaud-Sharma, A. McGoron, J. Biomater, Tissue Eng 12 (2012) 25–39.
[59] J.C. Bian, B.Y. Yu, J.F. Hao, H.W. Zhu, H.S. Wu, B. Chen, W.R. Li, Y.F. Li, L. Zheng, R.X. Li, China Foundry 19 (2022) 419–426.
[60] C.R. Ling, Q. Li, Z. Zhang, Y.W. Yang, W.H. Zhou, W.L. Chen, Z. Dong, C.R. Pan, C.J. Shuai, Int. J. Extreme Manuf. 6 (1) (2023) 015001.
[61] P. Saha, M. Roy, M.K. Datta, B. Lee, P.N. Kumta, Mater. Sci. Eng. C 57 (1) (2015) 294–303.
[62] Z. Li, X. Gu, S. Lou, Y. Zheng, Biomaterials 29 (10) (2008) 1329–1344.
[63] D. Li, D. Zhang, Q. Yuan, L. Liu, H. Li, L. Xiong, X. Guo, Y. Yan, K. Yu, Y. Dai, T. Xiao, Y. Li, C. Wen, Acta Biomater 141 (15) (2022) 454–465.
[64] Y.F. Zheng, X.N. Gu, Y.L. Xi, D.L. Chai, Acta Biomater 6 (5) (2010) 1783–1791.
[65] N. Safari, N. Golafshan, M. Kharaziha, M. Reza Toroghinejad, L. Utomo, J. Malda, M. Castilho, ACS Biomater. Sci. Eng 6 (11) (2020) 6253–6262.
[66] D.C. Martinez, A. Dobkowska, R. Marek, H. Ćwieka, J. Jaroszewicz, T. Płociński, Č. Donik, H. Helmholz, B. Luthringer-Feyerabend, B. Zeller-Plumhoff, R. Willumeit-Römer, W. Święszkowski, Bioact. Mater. 28 (2023) 132–154.
[67] W. Ci, X. Chen, X. Dai, C. Liu, Y. Ma, D. Zhao, F. Pan, J. Mater. Sci. Technol. 181 (10) (2024) 138–151.
[68] W. Jiang, A.F. Cipriano, Q. Tian, C. Zhang, M. Lopez, A. Sallee, A. Lin, M.C. Cortez Alcaraz, Y. Wu, Y. Zheng, H. Liu, Acta Biomater 72 (2018) 407–423.
[69] S. Lv, Q. Yang, X. Lv, F. Meng, X. Qiu, Mater. Des. 904 (25) (2022) 164040.
[70] D. Bian, J. Deng, N. Li, X. Chu, Y. Liu, W. Li, H. Cai, P. Xiu, Y. Zhang, Z. Guan, Y. Zheng, Y. Kou, B. Jiang, R. Chen, ACS Appl. Mater. Interfaces 10 (5) (2018) 4394–4408.
[71] Y. Li, Y. Yuan, J. Wang, L. Wu, F. Cao, L. Zhang, F. Pan, NPJ Mater. Degrad. 7 (1) (2023) 45.
[72] L. Xin, J. Zhou, D. Mei, P. Du, H. Qin, M. Bai, M. Liu, Y. Sun, S. Zhu, S. Guan, J. Alloy. Compd. 934 (10) (2023) 168044.
[73] Y.Z. Ma, D.X. Wang, H.X. Li, C.L. Yang, F.S. Yuan, J.S. Zhang, Trans. Nonferrous Met. Soc. China 31 (1) (2021) 111–124.
[74] H.R. Bakhsheshi-Rad, E. Hamzah, S.L. Joy Yii, A. Mostafa, R. Ebrahimi-Kahrizsangi, M. Medraj, Mater. Sci. Technol. 33 (11) (2017) 1333–1345.
[75] H.R. Bakhsheshi-Rad, M.H. Idris, M.R. Abdul-Kadir, A. Ourdjini, M. Medraj, M. Daroonparvar, E. Hamzah, Mater. Des. 53 (2014) 283–292.
[76] P. Duley, S. Sanyal, T.K. Bandyopadhyay, S. Mandal, Mater. Des. 164 (15) (2019) 139288.
[77] H.R. Bakhsheshi-Rad, M. Abdellahi, E. Hamzah, A.F. Ismail, M. Bahmanpour, J. Alloy. Compd. 687 (5) (2016) 630–642.
[78] Y. Wen, Q. Liu, J. Wang, Q. Yang, W. Zhao, B. Qiao, Y. Li, D. Jiang, Bioact. Mater. 6 (12) (2021) 4654–4669.
[79] H. Zhang, Y. He, J. Zhang, H. Dong, S. Liu, X. Jiao, R. Wu, X. Zhang, J. Alloy. Compd. 978 (25) (2024) 173473.
[80] L. Hou, Z. Li, H. Zhao, Y. Pan, S. Pavlinich, X. Liu, X. Li, Y. Zheng, L. Li, J. Mater. Sci. Technol. 32 (9) (2016) 874–882.
[81] K. Munir, J. Lin, X. Tong, A. Biesiekierski, Y. Li, C. Wen, J. Magnes. Alloy. 12 (2) (2024) 546–572.
[82] M.W. Vaughan, A.I. Karayan, A. Srivastava, B. Mansoor, J.M. Seitz, R. Eifler, I. Karaman, H. Castaneda, H.J. Maier, Mater. Sci. Eng. C 115 (2020) 111130.
[83] A. Kumar, P.M. Pandey, J. Magnes. Alloy. 8 (3) (2020) 883–898.
[84] Y. Li, H. Jahr, J. Zhou, A.A. Zadpoor, Acta Biomater 96 (15) (2019) 646–661.
[85] Q. Fu, W. Liang, J. Huang, W. Jin, B. Guo, P. Li, S. Xu, P.K. Chu, Z. Yu, J. Magnes. Alloy. 11 (5) (2023) 1485–1504.
[86] Y. Li, H. Jahr, X. Zhang, M. Leeflang, W. Li, B. Pouran, F. Tichelaar, H. Weinans, J. Zhou, A. Zadpoor, Addit. Manuf. 28 (2019) 299–311.
[87] J. Liu, B. Liu, S. Min, B. Yin, B. Peng, Z. Yu, C. Wang, X. Ma, P. Wen, Y. Tian, Bioact. Mater. 16 (2022) 301–319.
[88] K. Xie, N. Wang, Y. Guo, S. Zhao, J. Tan, L. Wang, G. Li, J. Wu, Y. Yang, W. Xu, Bioact. Mater. 8 (2022) 140–152.
[89] C. Shuai, Y. Li, P. Feng, W. Guo, W. Yang, S. Peng, Polym. Test. 68 (2018) 27–33.
[90] M. Jamalpour, R. Alizadeh, Intermetallics 165 (2024) 108133.
[91] J. Seong, W. Kim, Acta Biomater 11 (1) (2015) 531–542.
[92] A. Ercetin, D.Y. Pimenov, Materials (Basel) 14 (17) (2021) 4819.
[93] M. Li, H. Yuan, W. Ding, H. Du, X. Guo, D. Li, Y. Xu, J. Polym. Environ. 32 (2024) 4302–4431.
[94] X. Zhang, H. Shi, X. Wang, S. Zhang, P. Luan, X. Hu, C. Xu, J. Alloys Compd. 938 (25) (2023) 168567.
[95] D.H. Cho, D. Dean, A.A. Luo, J. Magnes. Alloy. 12 (7) (2024) 2711–2724.
[96] K.X. Kuah, D.J. Blackwood, W.K. Ong, M. Salehi, H.L. Seet, M.L.S. Nai, S. Wijesinghe, J. Magnes. Alloy. 10 (5) (2022) 1296–1310.
[97] D.G. Ahn, INT. J. PRECIS. ENG. MAN-GT 8 (2) (2021) 703–742.
[98] J.W. Li, Y.M. Qiu, J.J. Yang, Y.Y. Sheng, Y.L. Yi, X. Zeng, L.X. Chen, F.L. Yin, J.Z. Su, T.J. Zhang, X. Tong, B. Guo J. Magnes. Alloy. 11 (1) (2023) 217–229.
[99] W. Yang, H. Yang, K. Yang, X. Wang, C. Hu, X. Lin, J. Magnes. Alloy. 13 (3) (2025) 1187–1202.

[100] Y. Guo, G. Quan, Y. Jiang, L. Ren, L. Fan, H. Pan, J. Magnes. Alloy. 9 (1) (2021) 192–201.
[101] J. Hofstetter, E. Martinelli, A.M. Weinberg, M. Becker, B. Mingler, P.J. Uggowitzer, J.F. Löffler, Corros. Sci. 91 (2015) 29–36.
[102] H.X. Cao, M.T. Huang, C.C. Wang, S.Y. Long, J.L. Zha, G.Q. You, J. Magnes. Alloy. 7 (3) (2019) 370–380.
[103] B.C. Liu, S. Zhang, H.W. Xiong, W.H. Dai, Y.L. Ma, Acta Metall. Sin. 36 (1) (2023) 77–90.
[104] E. Landi, G. Logroscino, L. Proietti, A. Tampieri, M. Sandri, S. Sprio, J. Mater. Sci.: Mater. Med. 19 (2008) 239–247.
[105] C. Liu, Z. Ren, Y. Xu, S. Pang, X. Zhao, Y. Zhao, Scanning 2018 (1) (2018) 9216314.
[106] W. Jie, J.-X. Zhou, W.-H. Tong, Y.-S. Yang, Trans. Nonferrous Met. Soc. China 20 (7) (2010) 1235–1239.
[107] Q.C. Le, Z.Q. Zhang, J.Z. Cui, S.W. Chang, Mater. Sci. Forum, Trans Tech Publ 610 (2009) 754–757.
[108] Y. Feng, C. Liu, X. Huang, X. Zhang, Metall. Mater. Trans. B-Proc. Metall. Mater. Proc. Sci. 54 (5) (2023) 2467–2478.
[109] Y.H. Li, B. Song, N. Wang, Appl. Mech. Mater. 331 (2013) 421–426.
[110] F. Pan, X. Chen, T. Yan, T. Liu, J. Mao, W. Luo, Q. Wang, J. Peng, A. Tang, B. Jiang, J. Magnes. Alloy. 4 (1) (2016) 8–14.
[111] S. Shaikh, I. Qayoom, R. Sarvesha, A. Kumar, J. Magnes. Alloy. 11 (1) (2023) 270–286.
[112] M. Ali, M. Elsherif, A.E. Salih, A. Ul-Hamid, M. Hussein, S. Park, A.K. Yetisen, H. Butt, J. Alloys Compd. 825 (5) (2020) 154140.
[113] T.R. Rautray, R. Narayanan, K.H. Kim, Prog. Mater Sci. 56 (8) (2011) 1137–1177.
[114] X. Han, J. Ma, A. Tian, Y. Wang, Y. Li, B. Dong, X. Tong, X. Ma, Colloids Surf., B 227 (2023) 113339.
[115] H. Yang, K. Xia, T. Wang, J. Niu, Y. Song, Z. Xiong, K. Zheng, S. Wei, W. Lu, J. Alloys Compd. 672 (5) (2016) 366–373.
[116] Z.H. Xue, X.J. Sun, H. Li, M. Iqbal, L.J. Qi, F. Wang, Y.C. Hou, J.A. Li, S.K. Guan, J. Magnes. Alloy. 12 (11) (2024) 4547–4560.
[117] W. Wu, Z. Wang, S. Zang, X. Yu, H. Yang, S. Chang, ACS Omega 5 (2) (2020) 941–947.
[118] L. Li, D.D. Yan, T.T. Zou, J.P. Xu, R.Z. Zhang, L.J. Hu, J.J. Yang, J. Alloys Compd. 1004 (2024) 175728.
[119] Z. Chen, Z. Zhang, Y. Ouyang, Y. Chen, X. Yin, Y. Liu, H. Ying, W. Yang, Colloids Surf., A 662 (2023) 131041.
[120] B. Manne, H. Thiruvayapati, S. Bontha, R.M. Rangarasaiah, M. Das, V.K. Balla, Surf. Coat. Technol. 347 (15) (2018) 337–349.
[121] N. Pulido-González, B. Torres, M. Zheludkevich, J. Rams, Surf. Coat. Technol. 402 (25) (2020) 126314.
[122] J.Z. Lu, S.S. Joshi, M.V. Pantawane, Y.H. Ho, T.C. Wu, N.B. Dahotre, Mater. Sci. Eng. C 105 (2019) 110028.
[123] Q. Dong, Y. Jia, Z. Ba, X. Tao, Z. Wang, F. Xue, J. Bai, J. Alloys Compd. 873 (25) (2021) 159739.
[124] M. Jamesh, G. Wu, Y. Zhao, P.K. Chu, Corros. Sci. 69 (2013) 158–163.
[125] Y. Liu, D. Bian, Y. Wu, N. Li, K. Qiu, Y. Zheng, Y. Han, Colloids Surf., B 133 (1) (2015) 99–107.
[126] S. Somasundaram, M. Ionescu, B.K. Mathan, Metals (Basel) 8 (1) (2018) 30.
[127] H. Wang, S. Guan, X. Wang, C. Ren, L. Wang, Acta Biomater 6 (5) (2010) 1743–1748.
[128] Z.Q. Zhang, B.Z. Li, P.D. Tong, S.K. Guan, L. Wang, Z.H. Qiu, C.G. Lin, R.C. Zeng, J. Magnes. Alloy. 12 (1) (2024) 120–138.
[129] K. Akshay, V.M. Rabeeh, S.A. Rahim, K. Sijina, G. Rajanikant, T. Hanas, Surf. Coat. Technol. 448 (25) (2022) 128914.
[130] I. Antoniac, F. Miculescu, C. Cotrut, A. Ficai, J.V. Rau, E. Grosu, A. Antoniac, C. Tecu, I. Cristescu, Materials (Basel) 13 (2) (2020) 263.
[131] C. Yang, S. Cui, R.K. Fu, L. Sheng, M. Wen, D. Xu, Y. Zhao, Y. Zheng, P.K. Chu, Z. Wu, J. Mater. Sci. Technol. 179 (20) (2024) 224–239.
[132] T. Wang, G. Yang, W. Zhou, J. Hu, W. Jia, W. Lu, J. Alloys Compd. 799 (30) (2019) 71–82.
[133] Y.H. Zou, J. Wang, L.Y. Cui, R.C. Zeng, Q.Z. Wang, Q.X. Han, J. Qiu, X.B. Chen, D.C. Chen, S.K. Guan, Acta Biomater 98 (15) (2019) 196–214.
[134] M. Peng, F. Hu, M. Du, B. Mai, S. Zheng, P. Liu, C. Wang, Y. Chen, Front. Mater. Sci. 14 (2020) 14–23.
[135] C. Wang, Z. Yi, Y. Sheng, L. Tian, L. Qin, T. Ngai, W. Lin, Mater. Sci. Eng. C 99 (2019) 344–356.
[136] N.J. Ostrowski, B. Lee, A. Roy, M. Ramanathan, P.N. Kumta, J. Mater. Sci.: Mater. Med. 24 (2013) 85–96.
[137] L. Li, Z. Yang, X. Pan, B. Feng, R. Yue, B. Yu, Y. Zheng, J. Tan, G. Yuan, J. Pei, Adv. Funct. Mater. 32 (47) (2022) 2205634.
[138] C. Wang, B. Zhang, S. Yu, H. Zhang, W. Zhou, R. Luo, Y. Wang, W. Bian, G. Mao, J. Magnes. Alloy. 11 (11) (2023) 4247–4262.
[139] T. Wang, Y. Xu, Z. Liu, G. Li, Y. Guo, J. Lian, Z. Zhang, L. Ren, Prog. Org. Coat. 178 (2023) 107469.
[140] Y. Reyes, A. Durán, Y. Castro, Surf. Coat. Technol. 307 (15) (2016) 574–582.
[141] Y. Castro, A. Durán, J. Sol-Gel Sci. Technol. 90 (2019) 198–208.
[142] Y. Zhao, P. He, J. Yao, M. Li, J. Bai, F. Xue, C. Chu, Y. Cong, P.K. Chu, Adv. Healthcare Mater. 13 (9) (2024) 2302519.
[143] D. Xia, Z. Jia, Y. Shen, Y. Zheng, Y. Cheng, P. Xiong, S. Guan, Y. Xu, F. Yang, Y. Liu, Small 18 (36) (2022) 2106056.
[144] L. Li, F. Qi, Z. Zhang, L. Lu, X. Ouyang, Ceram. Int. 49 (3) (2023) 5327–5334.
[145] J. Dong, N. Tümer, M.A. Leeflang, P. Taheri, L.E. Fratila-Apachitei, J.M.C. Mol, A.A. Zadpoor, J. Zhou, J. Magnes. Alloy. 10 (9) (2022) 2491–2509.
[146] C. Wang, J. Liu, S. Min, Y. Liu, B. Liu, Y. Hu, Z. Wang, F. Mao, C. Wang, X. Ma, Bioact. Mater. 28 (2023) 537–548.
[147] A. Rezaei-Baravati, M. Kasiri-Asgarani, H.R. Bakhsheshi-Rad, M. Omidi, E. Karamian, S. Abazari, S. Sharif, A.F. Ismail, J.W. Drelich, J. Mater. Eng. Perform. (2024) 1–13.
[148] A.P. Md Saad, A.T. Prakoso, M.A. Sulong, H. Basri, D.A. Wahjuningrum, A. Syahrom, Biomech. Model. Mechanobiol. 18 (2019) 797–811.
[149] A. Yusop, A. Bakir, N. Shaharom, M. Abdul Kadir, H. Hermawan, Int. J. Biomater. 2012 (1) (2012) 641430.
[150] M.H. Kang, H. Lee, T.S. Jang, Y.J. Seong, H.E. Kim, Y.H. Koh, J. Song, H.D. Jung, Acta Biomater 84 (15) (2019) 453–467.
[151] Z. Qu, L. Liu, Y. Deng, R. Tao, W. Liu, Z. Zheng, M.C. Zhao, Materials (Basel) 15 (15) (2022) 5295.
[152] J. Hofstetter, M. Becker, E. Martinelli, A. Weinberg, B. Mingler, H. Kilian, S. Pogatscher, P.J. Uggowitzer, J.F. Löffler, JOM 66 (2014) 566–572.
[153] V. Roche, G. Koga, T. Matias, C. Kiminami, C. Bolfarini, W. Botta, R. Nogueira, A.J. Junior, J. Alloys Compd. 774 (2019) 168–181.
[154] Q. Ge, D. Dellasega, A.G. Demir, M. Vedani, Acta Biomater 9 (10) (2013) 8604–8610.
[155] S. Kamrani, C. Fleck, Biometals 32 (2019) 185–193.
[156] A.K. Khanra, H.C. Jung, K.S. Hong, K.S. Shin, Mater. Sci. Eng. A 527 (23) (2010) 6283–6288.
[157] S. Jaiswal, A. Dubey, D. Lahiri, Ceram. Int. 46 (17) (2020) 27205–27218.
[158] M. Haghshenas, J. Magnes. Alloy. 5 (2) (2017) 189–201.
[159] D.Q. Qin, X. Xiao, Y. Mao, X.C. Wang, L. Fu, J. Mater. Res. Technol. 24 (2023) 9141–9155.
[160] H. Tang, Y. Gao, J. Alloys Compd. 688 (2016) 699–708.
[161] C.S. Shao, L.J. Chen, R.M. Tang, B. Zhang, J.J. Tang, W.N. Ma, Rare Met 41 (2) (2022) 457–468.
[162] J. Dong, P. Lin, N. Putra, N. Tümer, M. Leeflang, Z. Huan, L. Fratila-Apachitei, J. Chang, A. Zadpoor, J. Zhou, Acta Biomater 151 (1) (2022) 628–646.
[163] J.L. Zhang, Q. Wu, C.C. Yin, X.S. Jia, Z.F. Zhao, X.X. Zhang, G.H. Yuan, H. Hu, Q. Zhao, J. Leukocyte Biol. 110 (3) (2021) 485–496.
[164] S.Y. He, S. Yue, M.F. Chen, D.B. Liu, X.Y. Ye, Trans. Nonferrous Met. Soc. China 21 (4) (2011) 814–819.

[165] M. Stein, F. Elefteriou, B. Busse, I.A. Fiedler, R.Y. Kwon, E. Farrell, M. Ahmad, A. Ignatius, L. Grover, L. Geris, J. Bone Miner. Res. 38 (8) (2023) 1045–1061.
[166] A.N. Jha, T.S. Kumaravel, T.N. Sathya, R. Balaje, P. Pradeepa, D. Yogaraj, M.R. Murali, K. Navaneethakrishnan, S. Murugan, Mutat. Res. Rev. Mutat. Res. 789 (2022) 108407.
[167] M. Mehdizade, A.R. Eivani, H. Asgari, Y. Naghshin, H.R. Jafarian, J. Mater. Res. Technol. 27 (2023) 852–875.
[168] J.W. Lee, H.S. Han, K.J. Han, J. Park, H. Jeon, M.R. Ok, H.K. Seok, J.P. Ahn, K.E. Lee, D.H. Lee, Proc. Natl. Acad. Sci. U. S. A. 113 (3) (2016) 716–721.
[169] I. Antoniac, R. Adam, A. Biță, M. Miculescu, O. Trante, I.M. Petrescu, M. Pogărășteanu, Materials (Basel) 14 (1) (2020) 84.
[170] D. Zhao, S. Huang, F. Lu, B. Wang, L. Yang, L. Qin, K. Yang, Y. Li, W. Li, W. Wang, Biomaterials 81 (2016) 84–92.
[171] D. Zhao, F. Witte, F. Lu, J. Wang, J. Li, L. Qin, Biomaterials 112 (2017) 287–302.
[172] C. Chen, J. Chen, W. Wu, Y. Shi, L. Jin, L. Petrini, L. Shen, G. Yuan, W. Ding, J. Ge, Biomaterials 221 (2019) 119414.
[173] J. Zhang, H. Li, W. Wang, H. Huang, J. Pei, H. Qu, G. Yuan, Y. Li, Acta Biomater 69 (15) (2018) 372–384.
[174] M. Bornapour, H. Mahjoubi, H. Vali, D. Shum-Tim, M. Cerruti, M. Pekguleryuz, Mater. Sci. Eng. C 67 (1) (2016) 72–84.
[175] R. Erbel, C. Di Mario, J. Bartunek, J. Bonnier, B.D. Bruyne, F.R. Eberli, P. Erne, M. Haude, B. Heublein, M. Horrigan, The Lancet 369 (9576) (2007) 1869–1875.
[176] P. Zartner, R. Cesnjevar, H. Singer, M. Weyand, Catheter. Cardiovasc. Interv. 66 (4) (2005) 590–594.
[177] M. Haude, R. Erbel, P. Erne, S. Verheye, H. Degen, D. Böse, P. Vermeersch, I. Wijnbergen, N. Weissman, F. Prati, The Lancet 381 (9869) (2013) 836–844.
[178] M. Haude, H. Ince, A. Abizaid, R. Toelg, P.A. Lemos, C. Von Birgelen, E.H. Christiansen, W. Wijns, F.J. Neumann, C. Kaiser, The Lancet 387 (10013) (2016) 31–39.
[179] X. Shan, Y. Xu, S.K. Kolawole, L. Wen, Z. Qi, W. Xu, J. Chen, J. Funct. Biomater. 13 (4) (2022) 298.
[180] M. Zhao, G. Liu, Y. Li, X. Yu, S. Yuan, Z. Nie, J. Wang, J. Han, C. Tan, C. Guo, Coatings 10 (5) (2020) 496.
[181] S. Zhang, X. Sun, C. Kang, M. Yang, Y. Zhao, C. Wang, Regener. Biomater. 7 (3) (2020) 331–336.
[182] P. Rider, Ž.P. Kačarević, A. Elad, D. Rothamel, G. Sauer, F. Bornert, P. Windisch, D. Hangyási, B. Molnar, B. Hesse, Materials (Basel) 15 (9) (2022) 3106.
[183] M. Blašković, I. Butorac Prpić, D. Blašković, P. Rider, M. Tomas, S. Čandrlić, D. Botond Hangyasi, M. Čandrlić, Ž.Perić Kačarević, J. Funct. Biomater. 14 (6) (2023) 307.
[184] Y.F. Zheng, X.N. Gu, F. Witte, Mater. Sci. Eng.: R: Rep. 77 (2014) 1–34.
[185] E. Mostaed, M. Sikora-Jasinska, J.W. Drelich, M. Vedani, Acta Biomater 71 (2018) 1–23.
[186] H.M. Garcia-Garcia, M. Haude, K. Kuku, A. Hideo-Kajita, H. Ince, A. Abizaid, R. Tölg, P.A. Lemos, C. von Birgelen, E.H. Christiansen, Int. J. Cardiol. 255 (15) (2018) 22–28.
[187] M. Haude, A. Wlodarczak, R.J. van der Schaaf, J. Torzewski, B. Ferdinande, J. Escaned, J.F. Iglesias, J. Bennett, G. Toth, M. Joner, EClinicalMedicine 59 (2023) 101940.
[188] P. Aprile, D. Letourneur, T. Simon-Yarza, Adv. Healthcare Mater. 9 (19) (2020) 2000707.
[189] K. Kim, Y. Su, A.J. Kucine, K. Cheng, D. Zhu, ACS Biomater. Sci. Eng. 9 (10) (2023) 5457–5478.
[190] A. Elad, P. Rider, S. Rogge, F. Witte, D. Tadić, Ž.P. Kačarević, L. Steigmann, Biomedicines 11 (3) (2023) 744.
[191] Q. Fu, C. Wang, C. Wu, Y. Wu, X. Dai, W. Jin, B. Guo, M. Song, W. Li, Z. Yu, J. Alloys Compd. 927 (2022) 167018.
[192] H. Zhou, J. Li, J. Li, Q. Ruan, W. Jin, Z. Yu, W. Li, P.K. Chu, Surf. Coat. Technol. 401 (2020) 126248.
[193] Q. Fu, M. Feng, J. Li, N. He, W. Li, J. Li, J. Yang, W. Jin, W. Li, Z. Yu, J. Coat. Technol. Res. 19 (6) (2022) 1757–1771.
[194] J. Li, J. Li, Q. Li, H. Zhou, G. Wang, X. Peng, W. Jin, Z. Yu, P.K. Chu, W. Li, Surf. Coat. Technol. 410 (25) (2021) 126940.
[195] J. Li, J. Li, N. He, Q. Fu, M. Feng, Q. Li, Q. Wang, X. Liu, S. Xiao, W. Jin, Colloids Surf., B 218 (2022) 112798.
[196] W. Jin, G. Wang, A.M. Qasim, S. Mo, Q. Ruan, H. Zhou, W. Li, P.K. Chu, Surf. Coat. Technol. 357 (15) (2019) 78–82.
[197] W. Jin, H. Zhou, J. Li, Q. Ruan, J. Li, X. Peng, W. Li, P.K. Chu, Chem. Phys. Lett. 756 (2020) 137824.
[198] X. Lin, J. Wang, N. Wu, M. Liu, H. Li, Y. Zhang, Q. Li, S. Xiao, W. Jin, Z. Yu, Colloids Surf., A 689 (20) (2024) 133678.
[199] Q. Fu, W. Jin, M. Feng, J. Li, J. Li, W. Li, Z. Yu, J. Magnes. Alloy. 11 (6) (2023) 2061–2071.
[200] Q. Fu, Z. Guo, D. Bo, K. Huang, Z. Su, W. Jin, Z. Yu, S. Xu, H. Li, Int. J. Polym. Mater. Polym. Biomater. 73 (13) (2024) 1126–1135.
[201] M. Feng, Q. Fu, J. Li, J. Li, Q. Wang, X. Liu, W. Jin, W. Li, P.K. Chu, Z. Yu, Colloids Surf., A 642 (5) (2022) 128647.
[202] N. He, J. Li, W. Li, X. Lin, Q. Fu, X. Peng, W. Jin, Z. Yu, P.K. Chu, Colloids Surf., A 661 (20) (2023) 130947.
[203] M. Feng, Q. Fu, J. Li, W. Jin, S. Xu, W. Li, Z. Yu, Metall. Mater. Trans. B-Proc. Metall. Mater. Proc. Sci. 55 (4) (2024) 1217–1228.
[204] Q. Fu, S. He, J. Yang, Z. Su, P. Li, X. Yu, W. Jin, S. Xu, Z. Yu, D. Zha, J. Magnes. Alloy. 12 (5) (2024) 2070–2089.
[205] H. Zhou, J. Li, J. Li, Q. Ruan, X. Peng, S. Li, W. Jin, Z. Yu, P.K. Chu, W. Li, Surf. Coat. Technol. 412 (25) (2021) 127078.
[206] J. Li, N. He, J. Li, Q. Fu, M. Feng, W. Jin, W. Li, Y. Xiao, Z. Yu, P.K. Chu, Surf. Coat. Technol. 439 (15) (2022) 128442.